POLITECNICO DI MILANO

Polo Regionale di Lecco

I Facoltà di Ingegneria Civile e Ambientale

Master of Science in Civil Engineering

DISCRETE ELEMENT MESOSCOPIC MODEL FOR TRIAXIAL BEHAVIOR OF CONCRETE

Silvio VERGA

Project Advisors:

- Francesco Calvetti — Politecnico di Milano
- Philippe Marin — Université Joseph Fourier, Grenoble
- Cedric Poinard — Université Joseph Fourier, Grenoble

Anno Accademico: 2009-2010

Abstract

The effects of natural and anthropogenic risks are often taken into account in the design of concrete safety structures, in order to deal with prediction of concrete structure response under severe loads such as impact. These impacts often induce phenomena of high deformation, cracks or fracturing, or even fragmentation. A dynamic impact can generate mean pressures around 1 *GPa*, but the characterization of a material response, in a homogeneous state of stress, can only be achieved through quasi-static tests. The aim of this work is to model the mechanical behavior of concrete under triaxial compression at the mesoscopic scale. At this scale concrete can be seen as three phase material composed of aggregates, mortar and pore. The more general scope of this study is to use the modeling of concrete behavior to better understand the damage mechanisms that create the failure of the specimen for high stress level.

Modeling concrete at the mesoscopic level, as a composite of an aggregates phase, mortar phase and porosity phase, permits to see the effects of heterogeneity. An experimental study of the behavior of each phase was performed. Axial compressive test, hydrostatic and triaxial at high confinement tests were realized. The parameters of a constitutive model that couples plasticity with a damage law are identified from these tests. This model is able to reproduce the damage behavior of concrete under uniaxial tension or compression, and plasticity under high confinement. Using these experimental results a discrete element model has been realized. To have a correct description of the concrete, tomographic scan have been done. Thanks to this we are able to reproduce numerically the concrete matrix.

Index

1 Introduction

Most of the major infrastructures are made of reinforced concrete or prestressed concrete like bridges, dams, nuclear power plant and are infrastructures that need defense proportional to their importance. If concrete is considered to offer a good resistance in this use of defense, quantifying the impact resistance or shock waves is an open subject. The phenomena prevailing in the concrete during an impact are well described, for example, by Zukas [1992] and Bailly [1996]. The conclusions of their work are given in Figure 1. It is noted in particular that during the penetration of the projectile, the state of stress is a state of triaxial compression. In front of the projectile, we have shear stress and tension so there is a multiaxial state of stress.

The main problem is to obtain an experimental measure of the response of concrete material under such dynamic loading, due to the transient and heterogeneous character of stress field in the sample. An approach that allows the quantification of this behavior is to use as a starting point a static study under very high confinement, fulfill by taking into account the effect of loading speed.

The 3S-R laboratory conducts, in collaboration with the CEA Gramat and DGA (Délégation Générale à l'Armement), a long-term study of the behavior of concrete under severe stresses. Under the cooperation agreement PREVI (Pôle de Recherche sur la Vulnérabilité des Infrastructures) between the DGA and Université Joseph Fourier, CNRS and INP Grenoble, the experimental part of this study was done with the use of a unique press, the GIGA press. This press was installed at the Laboratory 3S-R Saint-Martin-d'Hères, and was inaugurated in May 2004. His main interest is to study large samples of concrete (of the order of decimeter), which can be considered homogeneous until levels of mean stress in the order of 1 *GPa*.

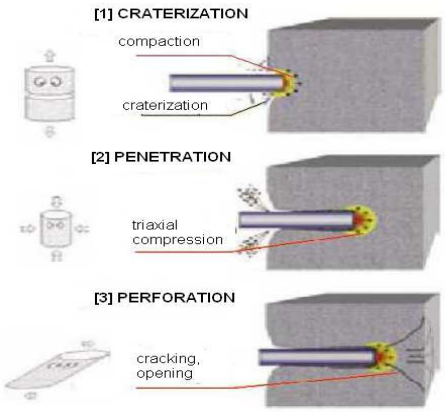

Figure 1 - Concrete under impact load, Bailly [1996]

1.1 Aim of the work

In previous works, simulations reproducing dynamic impact on structure have been done, with good results. In that kind of studies the numerical structure was homogeneous. Thanks to these works we have been able to simulate concrete slab. For more important structure it has been used a mixed method FE – DE [Rousseau, 2009]. This work instead is the beginning of a study that use discrete element method at the mesoscopic scale to understand better the damage mechanisms of concrete under triaxial load. This approach could also help to decrease the number of simulations. The simulations can be useful to see the influence of the three phases of concrete (mortar, aggregates and pore) at the mesoscopic scale. In particular one of the most important part is to define a properly percentage of these elements in the numerical mesh that corresponds to the percentage in the real specimen. The dimension of the representative volume does not allow us to use these results for the study of impact on structure. But from our work we will be able to have a better numerical sample that takes into account the heterogeneities of the real specimen. Starting from this study in future we will have the possibility to improve the simulation of dynamic impact on big structures.

2 Creation of the numerical mesh

One of the central parts of the work is the creation of a numerical sample that is as close as possible to the real one at the mesoscopic scale. In this section are detailed all the procedure followed to obtain the mesh used for the simulations.

2.1 Mortar and concrete composition

The creation of the real specimen has an important role in our work because it is from its composition that we can create a numerical sample. In the following are detailed the procedures to realize this specimen and in which way is found the percentage of every component at the mesoscopic scale.
As described in the study of Dupray [2008] the approach used is to separate the behavior of the three phases of the reference concrete R30A7 widely studied by Gabet [2006] and Vu [2007], to reunite them numerically in a triphasic model, composed of mortar, aggregates and porosity. Aggregates, given by the Sifraco society are compose for 98,7 % of silica with a density of 2630 kg/m^3. The sand, type Silmix, consists instead of 97,3 % silica. The mechanicals characteristics of aggregates and mortar are obtained by experimental tests.

The composition of the mortar MR30A7 is derived from the reference concrete R30A7, which have been subtracted aggregates of more than 2 *mm*. These aggregates correspond to the gravel used in concrete R30A7. A very small proportion of gravel (3 %) measured dimension less than 2mm. For the sake of simplicity, this part is replaced by an equal mass of sand from the lower class. The Table 1 gives the composition of concrete and mortar in kg/m^3

Material	Concrete R30A7	Mortar MR30A7
Composition for 1 m^3 of concrete		
Gravel D 2/8	1007 kg/ m^3	0 kg/ m^3
Sand 1,8 mm	838 kg/ m^3	1464 kg/ m^3
Cement CEM I 52,5	263 kg/ m^3	440 kg/ m^3
Water	169 l/ m^3	283 l/ m^3

Table 1 – Composition of concrete R30A7 and mortar MR30A7

The sample has 7 *cm* of diameter and a high just over 14 *cm*, without having problems in the test with Giga press if we remain in 1 mm over 14 *cm*.

From the beginning we already know the percentage of the three components of the concrete specimen. In particular the porosity due to air bubble, that is the one important for our work, is found with a compressibility test on fresh concrete obtaining these results:

- Mortar: 56.5 %
- Aggregates: 40 %
- Air bubble porosity: 3.5 %

We also have two other kinds of porosity, one at nanoscopic scale and one at microscopic scale, that are out of scale for our tomographic scan.

2.2 Tomographic scan and segmentation

The X-ray tomography is a non destructive method that allows measuring a physical parameter in 3D thanks to the emitted, transmitted and reflected radiation. It specially gives the 3D structure of objects by measuring the local density of materials presented in the object.

Our sample has been scanned using this technique with the XRay CT scanner installed in the Laboratory 3S-R.

The scan of our concrete specimen is realized considering the central part of the sample 5 *cm* high and with 7 *cm* of diameter. The images obtained have a resolution of 52 μm that permits a good description of the mesostructure (mortar, pore and aggregates) of the specimen. In particular, we have the scan of a central part of our sample, 5 *cm* high and 7 *cm* of diameter. These images are not yet useful for our work. These images in fact have to be segmented.

Segmentation refers to the process of partitioning a digital image into multiple segments (set of pixel, voxel in 3D). The goal of segmentation is to simplify and/or change the representation of an image into something that is more meaningful and easier to analyze. With image segmentation we are able to locate different element inside our sample basing on gray scale. More precisely, we assign a label to every pixel in an image such that, pixels with the same gray scale, belong to one of the three component of concrete. In particular in our segmented images we have different grey scale for each aggregates and only one for mortar and pore. The segmentation does not concern all the scanned part of the sample but only a representative cube of dimension 2,5 x 2,5 *cm*. This cube, named "A8-93", is the smallest one that maintains the same percentage of elements of the real one.

- Aggregates: 33,2 %
- Porosity: 3,4 %
- Mortar: 63.4 %

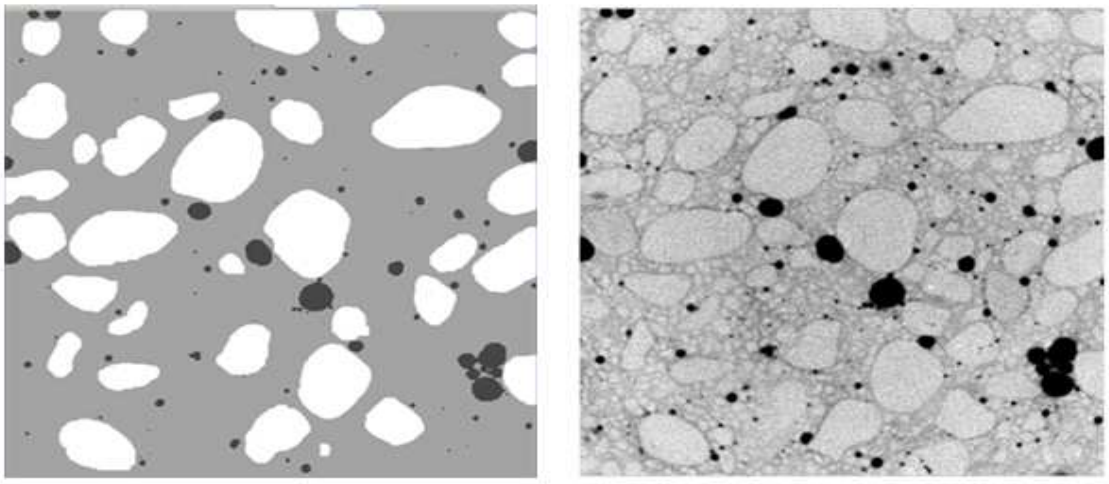

Figure 2 - Segmented slice, digital image

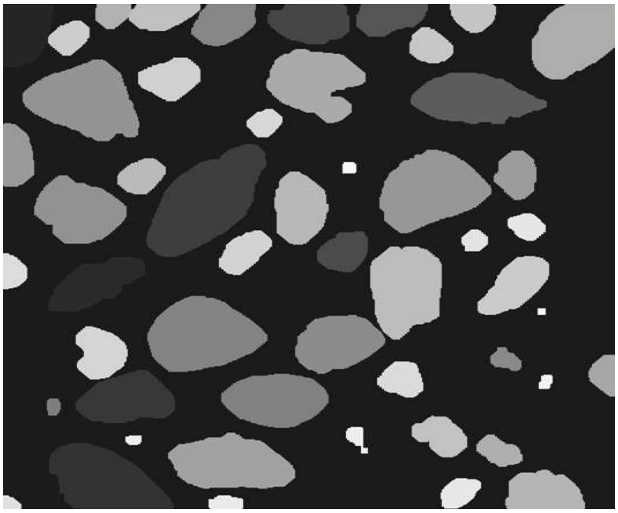

Figure 3 - Example of gray scale

These parts of the work were done by C. Poinard.

2.3 Numerical specimen

This part of the work starts from a cubic numerical mesh which has the same dimension of the segmented cube. The creation of the mesh has a very important role. First we have created a cubic tetrahedral mesh with a mesh generator called Gmsh. Then starting from a geometric algorithm, well described in the report of Jerier [2008], we create sphere assemblies where every tetrahedron is filled with sphere. This approach developed in six steps, can be presented trough an example on one tetrahedron:

Step 1: The first spheres are placed at the centre of the edges (Figure 4, Step 1), they are called Type 1 spheres. The values of six radii are fixed according to the length of edges:

$$radius = \frac{length(edges)}{k_1}$$

with the value k_1, an integer greater than zero, given by the user. If the user wants a sphere size distribution included between (R_{max}, R_{min}), he will have to define a mesh with length of the edges equal to k_1 times R_{avg} ($R_{avg} = \frac{R_{min} + R_{max}}{2}$).

Step 2: The spheres are placed on every vertex (Figure 4, Step 2), they are called Type 2 spheres. The four radii values are fixed according to the smallest distance $dist_1$ between the node and the centre of

Type 1 sphere and within the sphere size distribution imposed by the user (R_{max}, R_{min}). The radius of every Type 2 sphere is equal to:

$$radius = \frac{dist_1}{k_2}$$

with k_2 value defined by the user. Generally, the value of k_2 must be equal to the value of $k = \frac{k_1}{2}$

Step 3: The spheres are placed in an intermediate position, on every triangular face where they are in contact with the three non-aligned spheres (Type 1 and Type 2 spheres) placed on the same face. They are called Type 3 spheres (Figure 4, Step 3).

The spheres are fixed inside the packing under two conditions (user constraints):

- The radii values are within the chosen sphere size distribution (R_{max}, R_{min}).
- The sphere can slightly overlap other neighboring spheres.

Step 4: At this step, a sphere is placed at the centre of the tetrahedron using the geometric procedure; it is called a Type 4 sphere. If the user constraints are respected, the sphere is fixed inside the packing. Otherwise, the Type 4 sphere is rejected (Figure 4, Step 4).

Step 5: Four spheres are placed close to the tetrahedron vertices. These four spheres are called Type 5 spheres and they are each put in contact with a Type 2 sphere and three other neighbouring spheres because of the geometric procedure (Figure 4, Step 5), while respecting as for all the others, the user constraints.

Step 6: The spheres are added inside the packing to fill empty spaces while respecting the user constraints, these spheres are called Type 6 spheres.

To adjust the packing density value, there is some flexibility as the last three steps of the algorithm are independent from each other. Therefore, it is possible to adjust the packing density value by modifying or removing some of them.

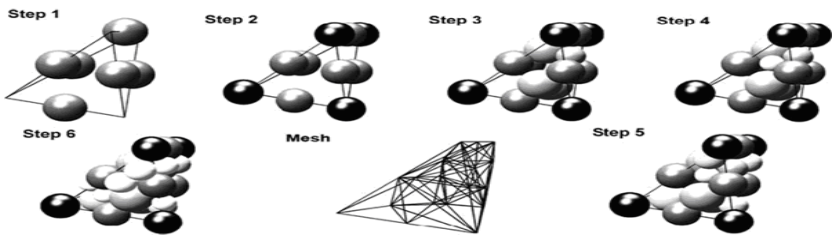

Figure 4 – Steps of the filling of a tetrahedron

Thanks to this algorithm we are able to generate an isotropic assembly as shown in Figure 5.

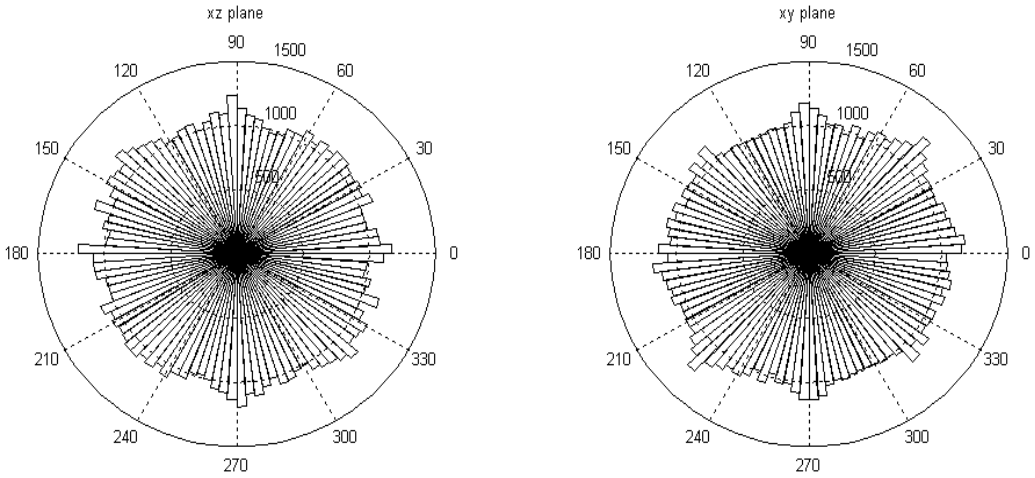

Figure 5 – Diagram of contact orientation

Having the mesh, to obtain a numerical sample as close as possible to the real one, we have matched the two cubes, the segmented one and the numerical one.

This matching is possible because we know the coordinates of every voxel and thanks to this we can assign each discrete element to a certain component: mortar, aggregate or pore. It is clear that is not possible to assign one voxel to one discrete element due to the number of spheres utilized in the numerical mesh that in this case are 9449.

In the following images there is a slice of the numerical cube obtained with ParaView. With this software we can see clearly the mesostructure of representative volume. White corresponds to mortar, red to aggregates and blue to porosity.

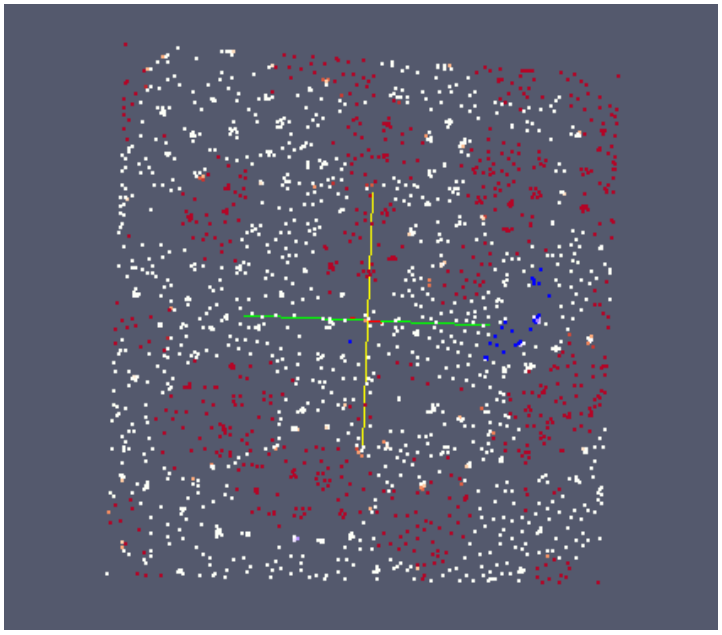

Figure 6 - Slice view of 9449 DE mesh

This representation could be improved with higher number of spheres as in the following where have been used 53784 DE.

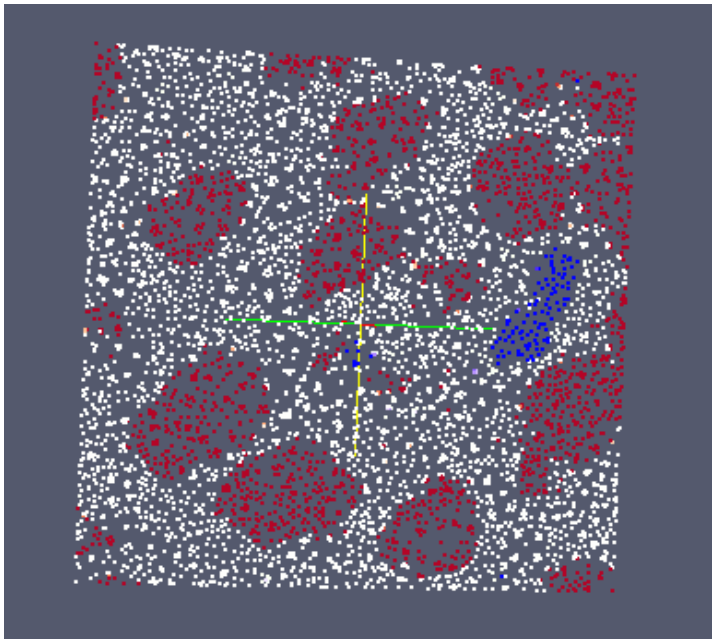

Figure 7 - Slice view of 53784 DE mesh

2.4 Sample representativity study

Once we have the numerical representative cube, our interest is to see if the real mesostructure is well represents in it. The following results concern the 9449 spheres mesh.

2.4.1 Porosity

First of all, as we already said previously, the tomographic scan can detect only the air bubble porosity and not all the porosity filled with water that is out of scale. Comparing the two curves, the one of the real specimen and the one of segmented cube we have the following results:

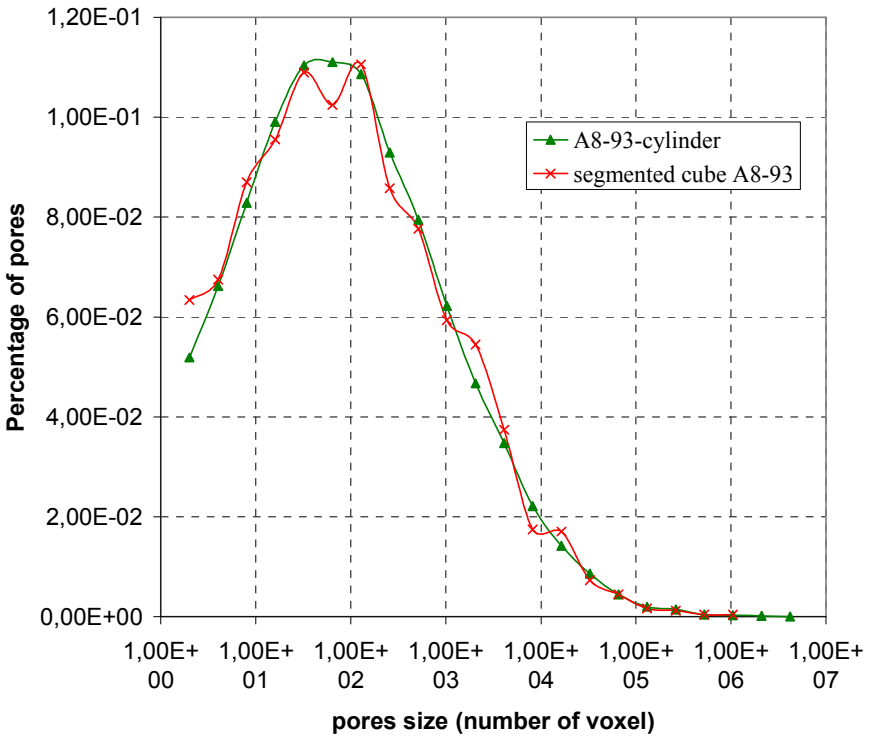

Figure 8 - Porosity comparison between real specimen and segmented cube

These results are obtained computing the distribution of porosity on the cylinder 5 *cm* high and with 7 *cm* of diameter and the distribution of porosity on the cube 2,5 x 2,5 *cm*. We can see that we have a good representation of the porosity in the segmented specimen.

If we consider our numerical mesh, we are able to represent only 5 % of the total number of air bubble pore of the segmented cube. However the global porosity is well represented. This is due to the fact that the pores that we cannot represent are not significant in the computing of global porosity due to the small size.

2.4.2 Aggregates

In the case of aggregates the comparison between the real specimen and the segmented cube is given from a sieve test and gives the following results:

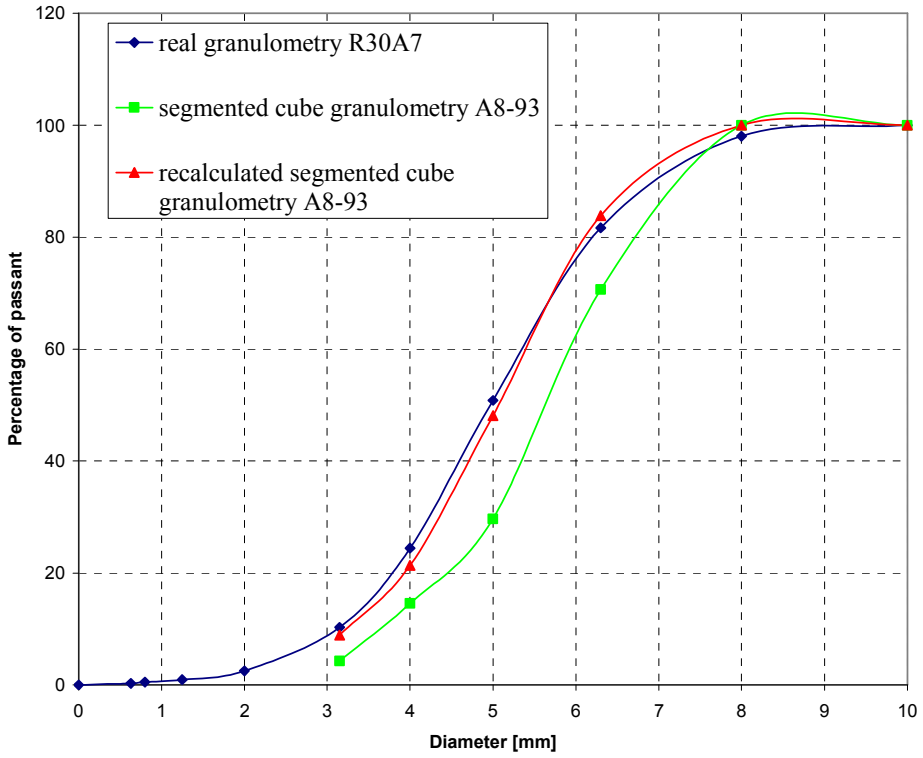

Figure 9 - Granulometric curves

In green we have the granulometric curve of the segmented cube and we can notice that it is not comparable with the curve of the real specimen. This happen because there is a wrong overestimation of the non passant. To overcome this problem we chose to take 45 % of aggregates of a class and

declass them. With such a correction we have a good representation of the granulometry for the segmented specimen.

Now that we know that also the granulometry of aggregates is well represented in our segmented cube we can study the numerical mesh.

From the following graph we compare the discrete elements corresponding to aggregates in the numerical cube and voxel corresponding to aggregates in the segmented ones:

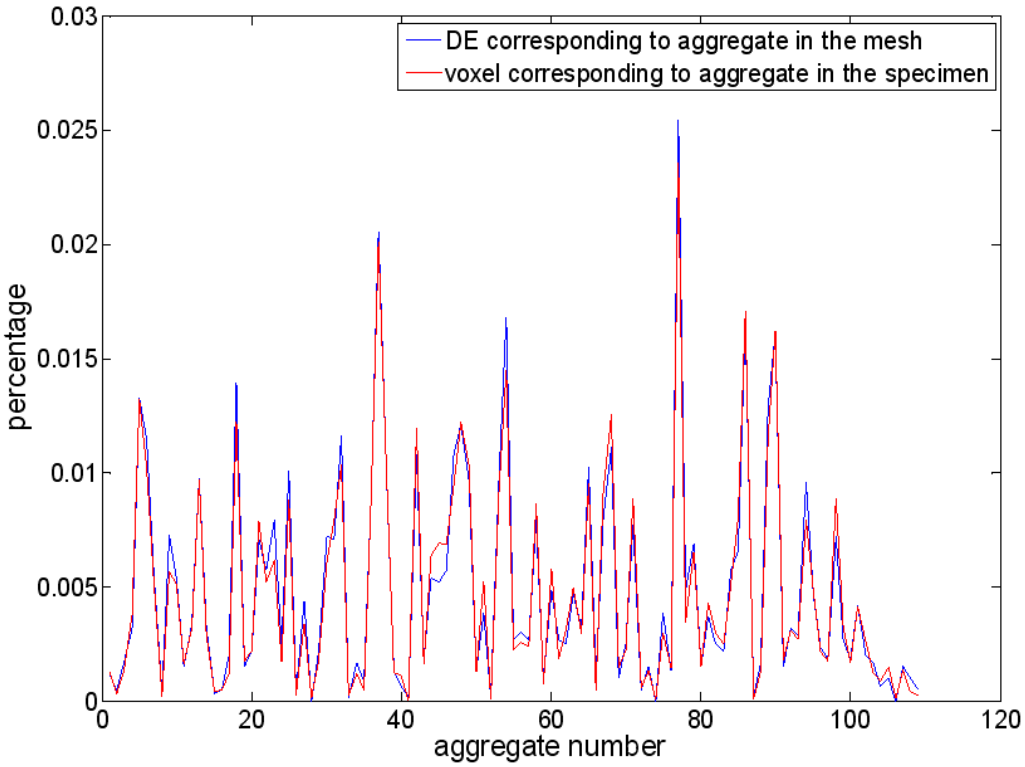

Figure 10 – representativity of aggregates

As we can see the representation of aggregates is close to the real one. We can now conclude saying that we can reproduce in a correct way the real structure of the specimen. Using MatLab we can also know the percentage of each element in our numerical cube.

- Mortar: 62,8 %
- Porosity: 3,6 %
- Aggregates: 33,6 %

2.4.3 Conclusion

A good representation of the mesostructure of concrete in terms of discrete element is not enough to reproduce the macroscopic behavior of this material. This behavior is governed by the repartition of the nature of the links. In the following table are detailed the percentages of links for each component:

Mesh 9449		Mesh 53784	
48 %	Mortar - Mortar	54,5 %	Mortar - Mortar
25 %	Mortar - Aggregate	15 %	Mortar - Aggregate
20 %	Aggregate - Aggregate (same aggregate)	25 %	Aggregate - Aggregate (same aggregate)
0,9 %	Aggregate - Aggregate (2 different aggregates)	0,1 %	Aggregate - Aggregate (2 different aggregates)
0,9 %	Pore - Pore	1,5 %	Pore - Pore
5,2 %	Pore - Mortar	3,9 %	Pore - Mortar

Table 2 – Repartition of links

In these kinds of interactions we can see that at first view the representation is not good enough. If we consider the percentage of links mortar – mortar we can notice that is lower than the percentage of mortar inside the segmented cube. This kind of interaction, in our computation, is governed obviously from the parameters of mortar. The same thing is for the links aggregate – aggregate, with discrete elements that belong to the same aggregate, in this case the interaction is governed by parameters of aggregates.

To overcome this problem of underestimation of links, we have to take into account aggregate – aggregate interaction, with two different aggregates that interact and mortar – aggregate interaction. The first one is governed by cohesion and tensile strength of mortar divided by a certain value (3 in our case) and the Poisson ratio and Young of mortar. This is due to the fact that there is always a layer of mortar between these aggregates in a real specimen. This interaction however is not going to affect strongly the behavior because of the low percentage of this kind of link. More important is the mortar – aggregate interaction because we have a significant percentage of this interaction. Its behavior is defined by cohesion and tensile strength of mortar also divided by 3 and the mean value of Poisson ratio and Young modulus of the two elements. We use this value to reduce these two parameters because the link “aggregate – mortar” is not as strong as the link mortar – mortar due to the fact in reality this boundary zone has poor mechanical properties. Considering also this interaction is very important because in our sample we have naturally links between two different components and

considering them we can have a good reproducibility of the behavior of concrete at the macroscopic scale. Better results about the representation of the nature of the links, are obtained increasing the number of spheres as we can see in Table 2. Although to improve our mesh we have to work on the representativity of the porosity. We can see in fact, that there is an overestimation of it. However we have to consider that this is only a beginning of this work and all these values can be improved in future in order to obtain a reproducibility of the concrete behavior that is close as possible to the real one.

3 Discrete element method

In the study of the simulation of an impact on a structure, it is important to take into account the phenomena of fracturing and fragmentation. To model concrete fragmentation, remain uneasy with continuous methods such as finite element. Cracks can't propagate anywhere; paths depend on the main directions of the mesh. To avoid this mesh dependency, we use a discrete element method which naturally describes discontinuities. These models have been developed primarily for modeling granular media for which the laws of contact between grains allow the description of the macroscopic behavior of the medium.

As well described in Rousseau [2009], discrete element methods are based on a rigid particle discretization of simple geometric form (like spheres). The material behavior is determined by the interaction law between the particles. They were first developed for non-cohesive geomaterials like sands [Cundall and Strack et al, 1979]. The particles then interact each other only by friction. The models were then enriched with stiffness.

The distinct element method [Cundall and Strack et al, 1979] is based on the use of a system of rigid spheres that interact through contact. The interactions between the spheres are managed by two stiffnesses, normal and tangential. They enable to obtain stresses, normal and tangential, for every contact and the total stress on every particle. The displacements are then calculated by applying the fundamental principle of dynamics. And the time integration is performed using an explicit scheme. Particle's shape is very important. Having spherical or circular particles have the advantage of allowing a very simple calculation of the schemes of contacts. However, in some configurations they tend to rotate easily. To solve this problem, other authors propose shape of particle more complex like ellipses or polyhedrons. Both of them have their drawback and especially the 3D modeling requires a very big computational effort.

Also, to take advantage from the spherical shape, Jensen [1999] and Salot [2007] combine several spherical particles inside a semi-rigid cluster in order to model a particle of the material. Clusters can represent finer particles shape of the material and so naturally model the compaction of the medium. Detection of contacts is facilitated for the spheres contained in each cluster. However, this method significantly increases the number of elements of the model.

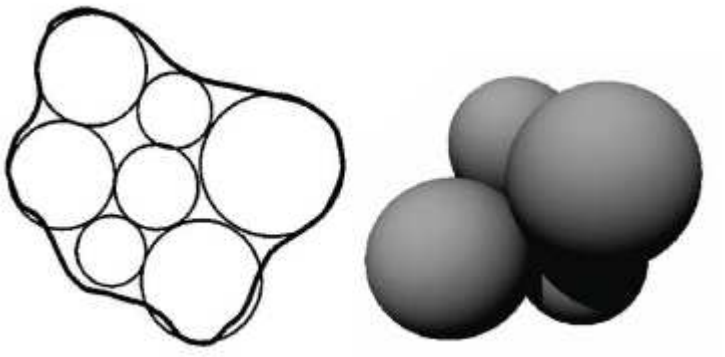

Figure 11 – Example of cluster in 2D ([Jensen et al., 1999]) and in 3D ([Salot et al, 2007)]

The results presented here were obtained with Sdec, a numerical discrete element code that use spherical elements, developed by F. Donzé. Recent works [Plassiard et al, 2007] have allowed adding in the code a moment/rotation low in 3D improving the capacity of modeling of the code.

In the previous chapter, we said that we use spherical elements. This choice is for reason of velocity when we are searching for contacts. The questions that arise now are: which are the characteristics needed to link discrete elements? What sizes of components to choose? A number of rules must be respected and these rules are described below.

3.1 General information

The simulations are done with a cubic sample of side 2,5 *cm*. Inside are placed 9449 spheres with radii that varies from $R_{min} = 3{,}69.10^{-4}$ *m* to $R_{max} = 1.108.10^{-3}$ *m* (Figure 12).

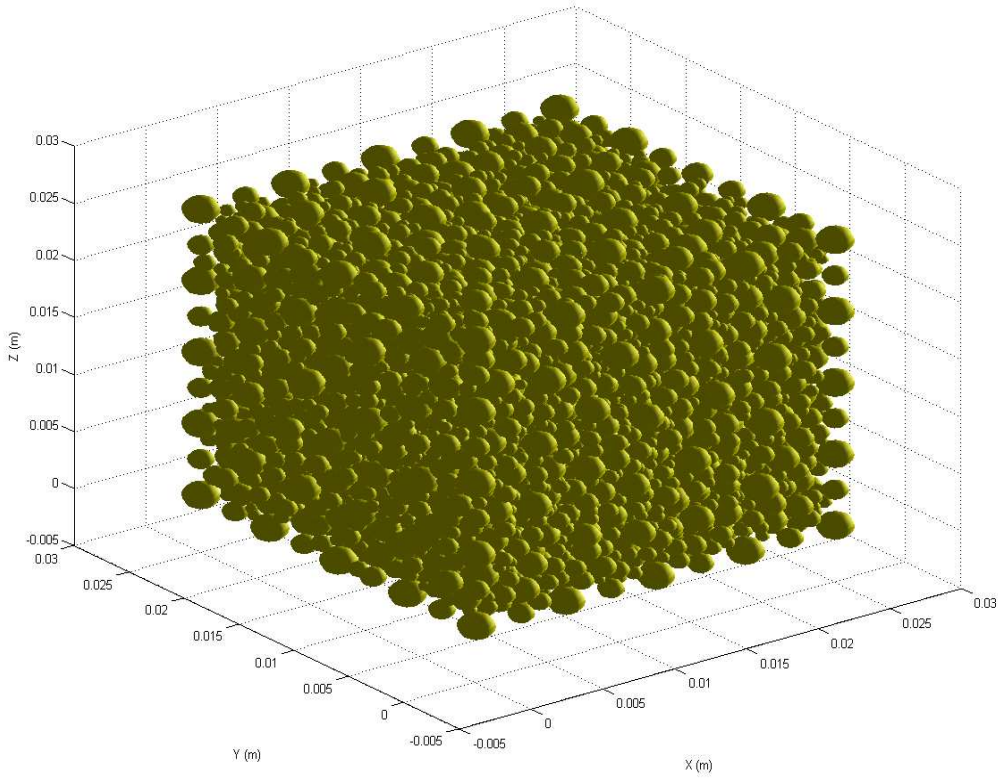

Figure 12 – Numerical sample

3.1.1 Computation of velocity

The sample is subjected to different solicitations. We call *m* the element's mass, *G* its center and *R* its radius. $\vec{u}$ is the displacement of the element. Each DE has six degree of freedom that corresponds to three translations and three rotations. The computation cycle is described in Figure 13. It starts taking into account a first phase of research of the interactions between elements. Then the interaction forces are computed using local laws. Subsequently we compute the sum of the interaction forces acting on each element $F_{tot} = \sum F_{loc}$.

In the end we integrate the fundamental principle of dynamic $F_{tot} = m\ddot{u}$ with an explicit scheme as shown in [3.1].

$$\begin{cases} \dot{u}^{n+1} = \dot{u}^{n} + \dfrac{\Delta t}{2}\left(\ddot{u}^{n} + \ddot{u}^{n+1}\right) \\ u^{n+1} = u^{n} + \Delta t\left(\dot{u}^{n} + \dfrac{\Delta t}{2}\ddot{u}^{n}\right) \end{cases} \tag{3.1}$$

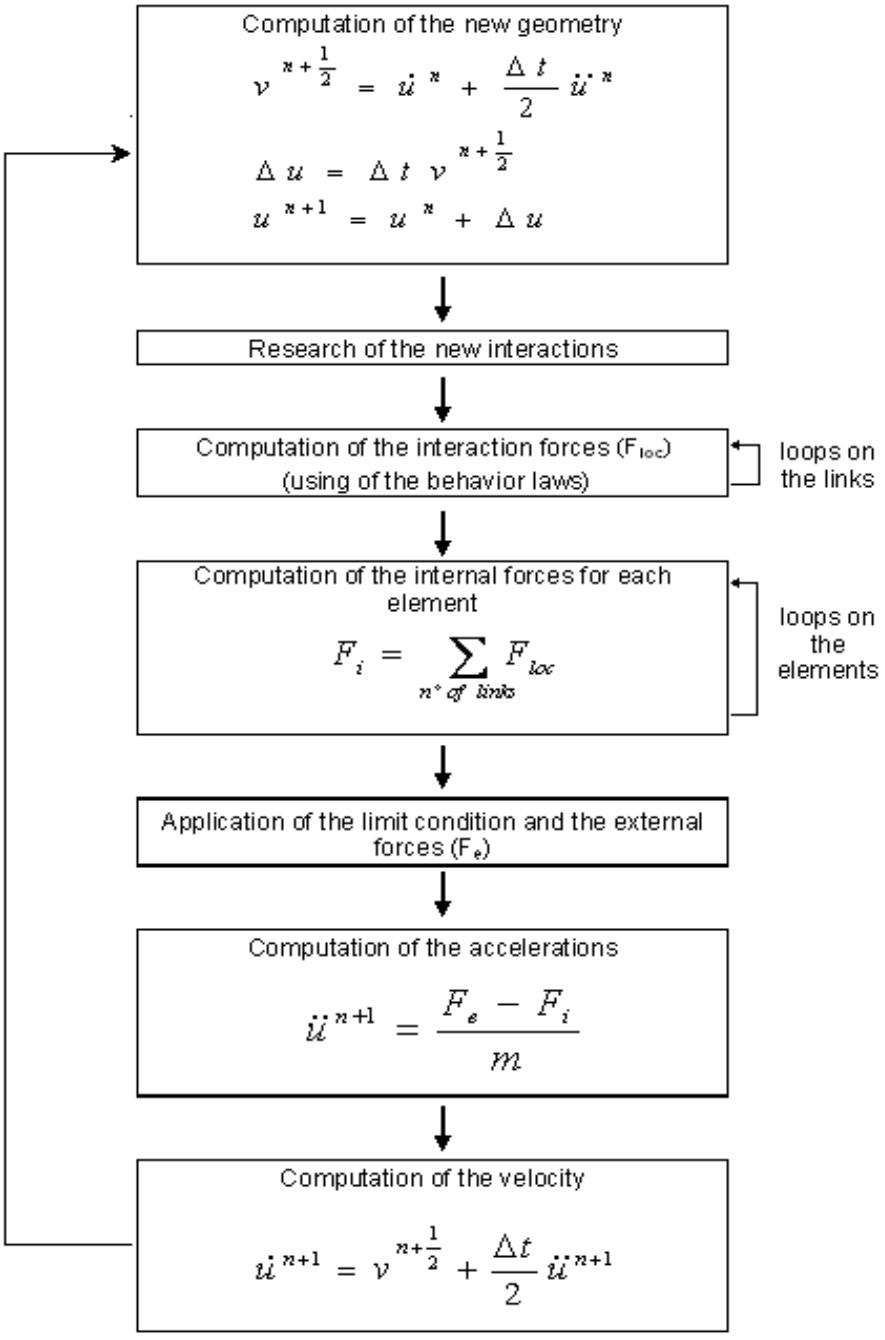

Figure 13 – computation loop for the DE

3.1.2 Definition of interaction

The discrete element method is therefore based on spherical rigid interaction. Two kinds of interactions are defined: contact interactions and cohesive interactions.

An interaction of type contact exists if two elements are in strict contact that means when the distance between the two is less than the sum of their radius. If both elements are no longer in contact, so the link is broken, these links have no resistance to traction. Instead, cohesive interactions are links with a certain tensile strength to model cohesive materials such as concrete. These interactions can be defined with an interaction radius.

The cohesive interactions are usually generated at the initial instant while contact interaction during the calculation between two elements initially separated or separated after the cohesive interaction is broken. The definition of interactions requires a research algorithm of neighboring elements very effective. This research phase of new interactions is a major part of computation time. There are several research methods include for example the method of sorting by grid or by stacking [Hentz et al., 2003].

The method of stacking classifies elements according to their coordinates. The extreme coordinates of the element, for which we search contacts, define bands and we research interactions between the elements intersected by these bands (Figure 14). These methods are insensitive to the size of the elements.

The sorting method by grid discretized the space into cells and their associated elements they contain. Then we search therefore the contacts between an element and all other elements of the cell and of adjacent cells (Figure 15). The cell size then determines the cost of this operation. It is therefore very sensitive to the size distribution of elements but very efficient for compact samples. This is the case of applications referred to using dense samples and with relatively small variations in size. This method of sorting grid has been established in Sdec.

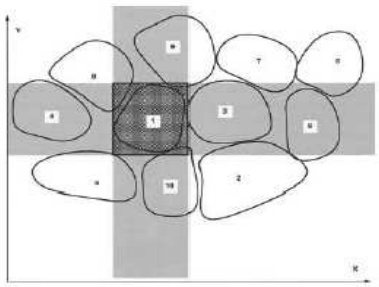

Figure 14 – Stacking method

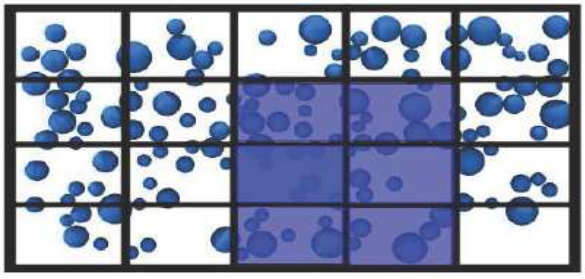

Figure 15 – Grid method

3.1.3 Computation of the interaction forces

For each interaction (Figure 16), we define a normal $\vec{N}$ between the centers G_a and G_b of both elements *a* and *b*. The distance between the two elements is called D_{ab} and at the initial time it will be noted D_{eq}. It also defines a fictitious contact point P_c at equal distance from the surface of the two elements: $\overrightarrow{G_a P_c} = \left(R_a + \frac{1}{2}\left(D_{ab} - \left(R_a + R_b\right)\right)\right)\vec{N}$

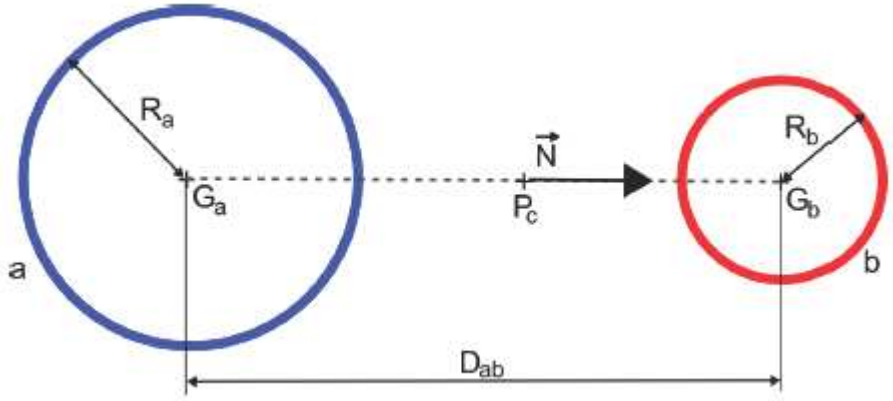

Figure 16 – Definition of the interaction parameters

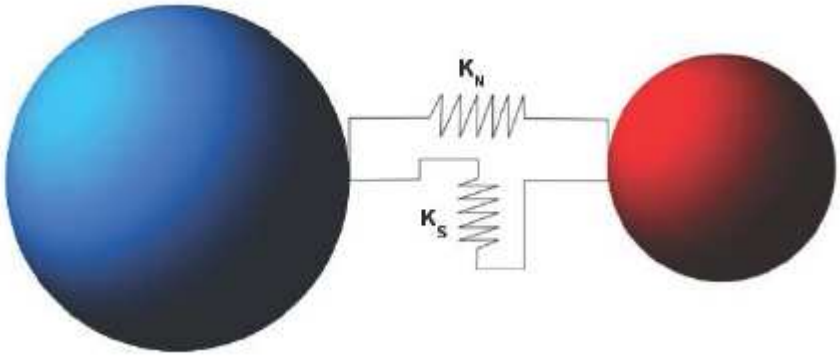

Figure 17 – Interaction between two elements

The interaction force is divided into two parts: a normal force F_n and a tangential force F_s. We define two stiffness: normal K_n and tangential K_s (Figure 17).

Then the normal force is calculated as:

$$\overrightarrow{F_n} = -K_n\left(D_{ab} - D_{eq}\right)\overrightarrow{N} \tag{3.2}$$

Note $F_s(i)$ the tangential force at time i. The tangential force is calculated in an incremental way as the sum of the increment of the tangential force ΔF_s tangential and of the tangential force note as F_s^{rot2} [Hart et al., 1988].

$$\overrightarrow{F_s(i)} = \overrightarrow{\Delta F_s} + \overrightarrow{F_s^{rot2}} \tag{3.3}$$

The tangential force noted F_s^{rot2} is the updating of the tangential force at previous step. It is calculated in two steps. At first, we take into account the change in direction of the normal $\vec{N}$:

$$\overrightarrow{F_s^{rot1}} = \overrightarrow{F_s(i-1)} - \overrightarrow{F_s(i-1)} \cap \overrightarrow{N(i-1)} \cap \overrightarrow{N(i)} \tag{3.4}$$

In a second step, we take into account the average rotational speed $\vec{\Omega}$ according to the new normal:

$$\overrightarrow{F_s^{rot2}} = \overrightarrow{F_s^{rot1}} - \overrightarrow{F_s^{rot1}} \cap \Delta t\vec{\Omega} \tag{3.5}$$

With: $$\vec{\Omega} = \left(\frac{1}{2}\left(\overrightarrow{\Omega_a} + \overrightarrow{\Omega_a}\right) \cdot \overrightarrow{N(i)}\right)\overrightarrow{N(i)} \tag{3.6}$$

Then, it computes the increment of the shear force:

$$\overrightarrow{\Delta F_s} = -K_s\overrightarrow{\Delta u_s} \tag{3.7}$$

With the increment of tangential displacement Δu_s calculated from the relative velocity between the two elements at the contact point Pc.

$$\begin{cases} \overrightarrow{\Delta u_s} = \Delta t\overrightarrow{V_s^c} \\ \overrightarrow{V_s^c} = \overrightarrow{V^c} - \left(\overrightarrow{V^c} \cdot \overrightarrow{N}\right)\overrightarrow{N} \end{cases} \tag{3.8}$$

The relative velocity at point P_c is computed as:

$$\overrightarrow{V_s^c} = \overrightarrow{V_b^c} - \overrightarrow{V_a^c} \tag{3.9}$$

We can obtain now the total interaction force $\overrightarrow{F_{tot}} = \overrightarrow{F_n} + \overrightarrow{F_s}$. This force is applied on the element *a* and *b* with opposite signs.

3.1.4 Choice of time step

Using an explicit scheme leads to instabilities if the time step chosen is too large or too small. The equations to solve for a system composed of discrete elements can be compared to those obtained for a sum of mass-spring system (mass *m* and stiffness *k*) with a degree of freedom. The angular frequency of each system is $\omega = \sqrt{\frac{k}{m}}$. There is a stability condition for integration through the explicit scheme for this system with one degree of freedom undamped ([Geradin and Rixen, 1993]):

$$\Delta t \leq \frac{2}{\omega} \tag{3.10}$$

To respect this condition, it should therefore calculate the highest angular frequency of the system. This approach is not possible in our case where the assembly concern a great number of elements each subject to several interactions. We could compute this frequency by taking the smallest mass and the highest stiffness but this method may be too restrictive.

We have therefore chosen to calculate for each element an equivalent stiffness K_{eq} from all the interactions acting on this element. Therefore we obtained six equivalent stiffness projected in each direction (3 translations and 3 rotations). Then we have just to calculate the critical time step in each direction and for each element. Finally, we choose the smallest not found. To satisfy the stability condition, the time step is calculated as in Equation 3.11. For security reasons we use also a weighting parameter $0 \leq p \leq 1$.

$$\Delta t = \frac{p}{\omega} = p\sqrt{\frac{m}{K_{eq}}} \tag{3.11}$$

3.1.5 Computation of discrete elements mass

If the mass of each element is calculated as the volume element (sphere) multiplied by the density, then the total mass of the system will be not properly respected, because of the small compactness c in the sample. To overcome this problem, the mass of each element m is corrected to obtain the actual mass of the sample.

$$m = \frac{\rho}{c}\frac{4}{3}\pi R^3 \tag{3.12}$$

3.1.6 Interaction radius

The interaction radius λ, used for the creation of cohesive links, allow us to define the discrete elements that will interact. If we consider two elements *a* and *b*, they are going to interact if the condition [3.13] is respected. This does not mean that the two elements are in strict contact.

$$\lambda = (R_a + R_b) \geq D_{a,b} \quad with \quad \begin{cases} D_{a,b}\ dis\tan ce\ between\ two\ elements \\ R_a\ et\ R_b\ radii\ of\ the\ elements \end{cases} \tag{3.13}$$

By adjusting the interaction radius, we can set the desired number of interaction (Figure 14). Subsequently, the average number of interaction for element is called coordinance [3.14]. This parameter is very important because it determines the elastic behavior of the material.

$$Coordinance = \frac{n°\ of\ links}{n°\ of\ elements} \tag{3.14}$$

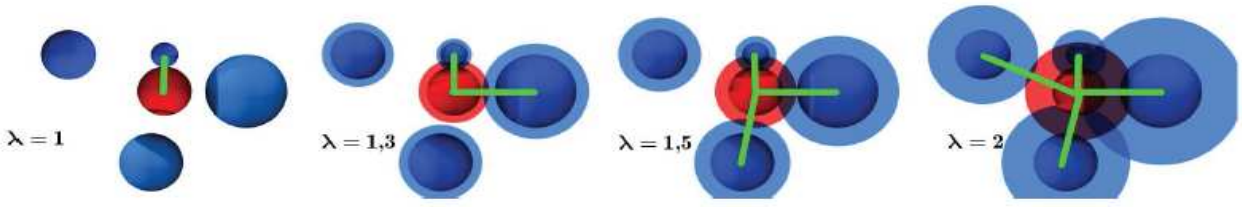

Figure 18 – Number of link in function of the interaction radius

3.1.7 Measure of deformation

The deformations of the sample are calculated from the average deformation of it. For better stability, the radial deformations are measured away from the edges of the elements (unstable) and the center of the sample (to avoid values near 0), as it is shown in Figure 19.

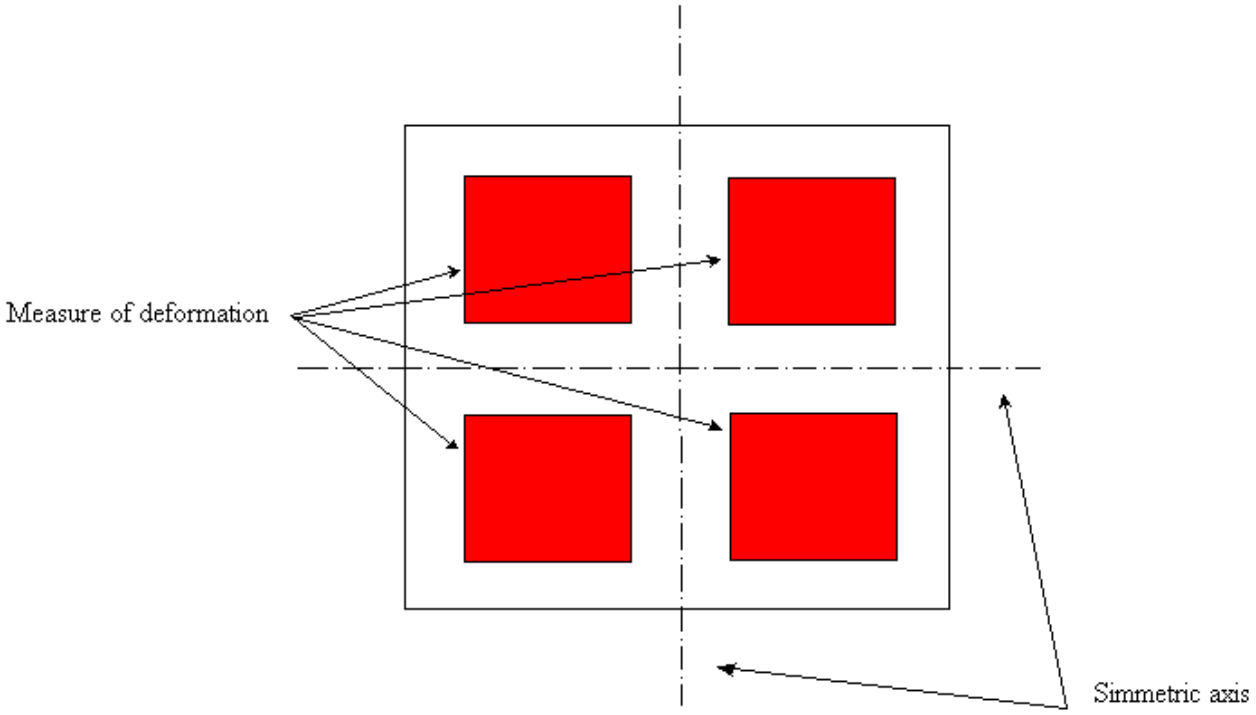

Figure 19 – Measure of deformation

3.2 Modelization of concrete

3.2.1 Elasticity

In the discrete element model used [Hentz, 2003], interactions between spheres are defined by a normal stiffness K_n and a tangential stiffness K_s. These values have to represent the elastic behavior of concrete and they are calculated starting from a "micro-macro" relation [3.15] function of the macroscopic parameters E and ν. These relations come from homogenization models of Voigt [3.16] and Liao [3.17] used for regular assemblies. They have been adapted to a disorderly assembly with elements of different sizes using a surface interaction S_{int} and the parameters α, β, γ that have to be determined.

S_{int} is the minimum surface of two elements when they interact: $S_{int} = min\ (\pi R^2_a, \pi R^2_b)$.

D_{eq} is the equivalent distance between particles.

$$\begin{cases} E = \dfrac{D_{init}^{a,b}}{S_{\text{int}}} K_n \dfrac{\beta + \gamma \dfrac{K_s}{K_n}}{\alpha + \dfrac{K_s}{K_n}} \\ \nu = \dfrac{1 - \dfrac{K_s}{K_n}}{\alpha + \dfrac{K_s}{K_n}} \end{cases} \quad where \quad \begin{cases} K_n = E \dfrac{S_{\text{int}}}{D_{init}^{a,b}} \dfrac{1+\alpha}{\beta(1+\nu) + \gamma(1-\alpha\nu)} \\ K_s = K_n \dfrac{1-\alpha\nu}{1+\nu} \end{cases} \tag{3.15}$$

$$\begin{cases} E = \dfrac{4Nr^2}{3} K_n \dfrac{2 + 3\dfrac{K_s}{K_n}}{4 + \dfrac{K_s}{K_n}} \\ \nu = \dfrac{1 - \dfrac{K_s}{K_n}}{4 + \dfrac{K_s}{K_n}} \end{cases} \quad \begin{array}{l} Voigt\ \text{model} \\ N = number\ of\ elements\ per\ unit\ volume \\ r = radius\ of\ the\ elements \end{array} \tag{3.16}$$

$$\begin{cases} E = \dfrac{20Nr^2}{3} K_n \dfrac{\dfrac{K_s}{K_n}}{2 + 3\dfrac{K_s}{K_n}} \\ \nu = \dfrac{1 - \dfrac{K_s}{K_n}}{2 + 3\dfrac{K_s}{K_n}} \end{cases} \quad Liao\ \text{model} \tag{3.17}$$

The values of α, β, γ come from the study of Rousseau [2009] where they are identified from quasi-static uniaxial elastic compression test made on a representative elementary volume of concrete.

$$\begin{cases} \alpha = 3{,}7 \\ \beta = 2{,}198 \\ \gamma = 3{,}79 \end{cases}$$

We should have also to adjust the interaction radius so that the number of interactions between an element and all its neighbors is 12. The number 12 was chosen because it corresponds to the average

number of contacts for element, for a regular three-dimensional mesh, type Cubic-Face-Centered, which ensures that there will be neither too much nor too less interaction.

3.2.2 Non-Linearity

Defined the elastic characteristics is important to represent the non-linear behavior of concrete [CEG/DGA and 3S-R, 2007]. In the case of cohesive interaction, the local criterion used is a standard Mohr-Coulomb criterion for the modeling of concrete. This criterion f_1 is defined for an internal friction angle Φ_i and for cohesion parameter C_0 [3.18]. A tensile rupture criterion is added to taking into account the fragility in traction f_2 [3.18]. We define T as the local tensile limit (Figure 20). F_n and F_s are the tangential and normal loads.

$$\begin{cases} f_1(F_n, F_s) = F_s - \tan(\phi_i) F_n - S_{\text{int}} C_0 & (\textit{sliding criterion}) \\ f_2(F_n, F_s) = S_{\text{int}} T - F_n & (\textit{tensilerupturecriterion}) \end{cases} \tag{3.18}$$

The criteria are written then:

$$\begin{cases} \textit{if} \quad f_2(F_s, F_n) \le 0 & \textit{cohesive and elasticlic link} \\ \textit{if} \quad f_1(F_s, F_n) \ge 0 \textit{ and } f_2(F_s, F_n) < 0 & F_s = \tan(\phi_i) F_n - S_{\text{int}} C_0 \\ \textit{if} \quad f_2(F_s, F_n) < 0 & \textit{rupture} \ (F_s = F_n = 0) \end{cases} \tag{3.19}$$

It's to be noted that a softening factor ζ is introduced in tension (Figure 12) to make the tensile force progressively tend to zero. When ζ tend to 0 the behavior is more brittle.
If an unload occurs during the softening phase, the unloading is done without residual deformation in accordance with what is observed when the concrete is under unload [3.21].

$$\begin{cases} F_n = \dfrac{K_N}{\varsigma} (D_{ab} - D_{\max}) \\ D_{\max} = D_{eq} + (1 + \varsigma) \dfrac{S_{\text{int}} T}{K_N} \\ K_{N2} = \dfrac{F_n}{(D_{ab} - D_{eq})} \end{cases} \tag{3.20}$$

$$F_n = -K_{N2}\left(D_{ab} - D_{eq}\right) \tag{3.21}$$

When the cohesive link is broken, a contact interaction can appear between the two elements. A law as in the [3.22] is used with $C_0 = T = 0$ and a contact angle Φ_c.

$$f_1\left(F_n, F_s\right) = F_s - \tan\left(\phi_c\right)F_n \tag{3.22}$$

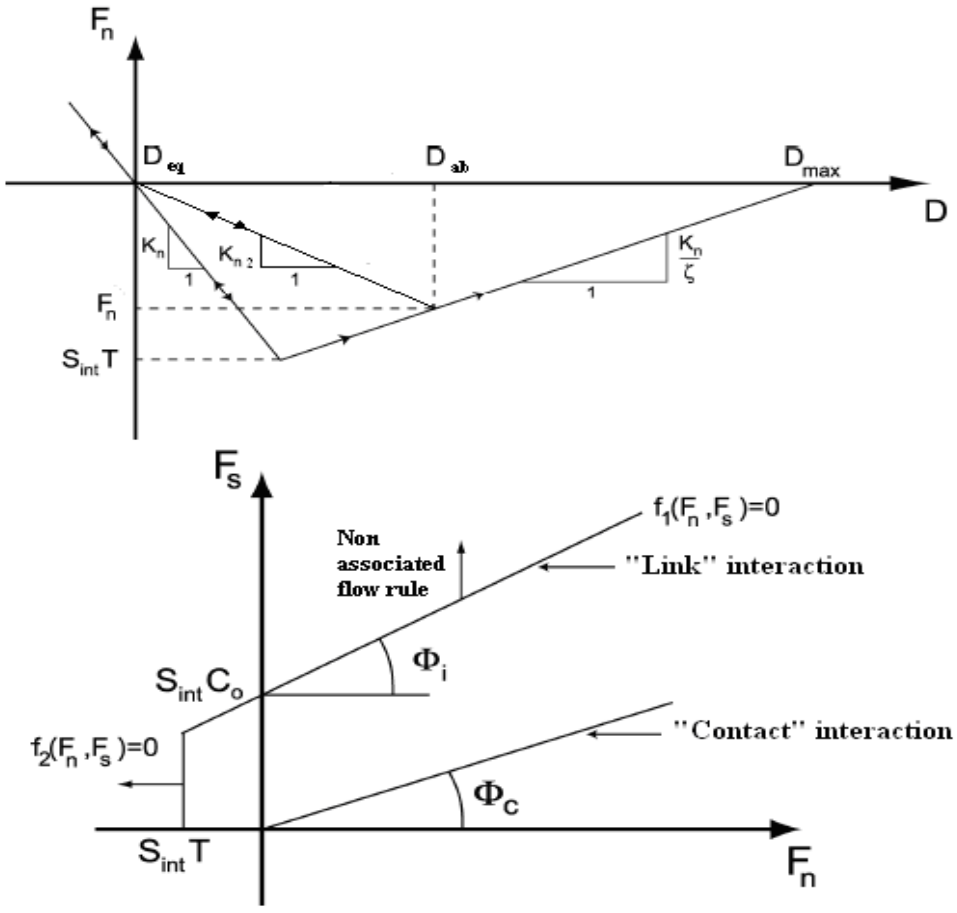

Figure 20 – Interaction law

This is a first simple model of asymmetric and brittle behavior of concrete. It has been refined by taking into account inelastic deformation due to compaction of concrete under high triaxial stress.

3.2.3 Compaction

The previous model can be improved taking into account the concrete compaction. In fact the normal stiffness remained constant and the failure criterion was for the traction. When concrete is under high confinement, the phenomenon of compaction appears and that model is not sufficient to properly represent it. If, for example, we consider the hydrostatic test, we can observe a decrease of stiffness associated with decohesion of the cement structure followed by a significant increase due to the closure of porosity. Then we can propose the following model:

Normal stiffness: a linear elastic spring of stiffness K_n of the previous model is coupled in series with a slider limiting the load transmitted without cohesion in compression of the cement matrix (in practice the force depends on the radius of the discrete element concerned and sliding will occur when it exceeds a value of deformation ε_{max}). This set is coupled in parallel with a non-linear spring stiffness K_{n2} that is activated starting from a normal strain value ε_{jeu}.

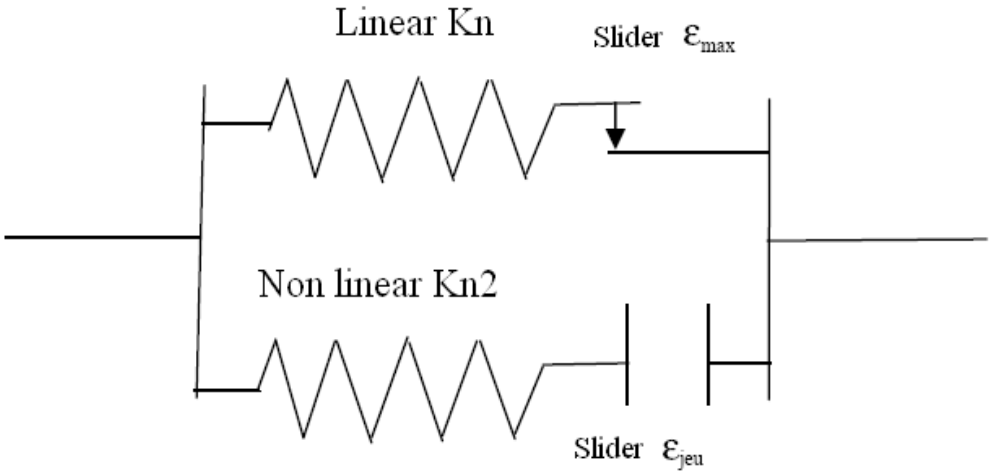

Figure 21 – Rheological model

The non-linear normal stiffness K_{n2} can be written as following:

$$K_{n_2} = K_n \cdot \left[a \cdot \left(1 - e^{-b\left(\varepsilon - \varepsilon_{jeu}\right)} \right) + c \right] \tag{3.23}$$

The parameter *c* will drive the slope at the early phase of compaction and the sum *a* + *c* is the slope at the end of compaction phase. The parameter *b* will control the curvature of the curve of compaction. These parameters have been identified from the hydrostatic test.

Tangential stiffness: If we keep the previous model for the tangential part and we couple it with the new model for the normal part, the radial deformation at high pressure remains too low for proportional tests. To increase this strain we changed the sliding criterion by limiting the increase of the maximum possible shear force.

$$\begin{cases} f_1(F_n,F_s) = F_s - F_n \cdot \tan(\phi_i) - S_{\text{int}} \cdot C_0 = 0 \\ f_3(F_n,F_s) = F_s - S_{\text{int}} \cdot C_0 \end{cases} \tag{3.24}$$

f_1 is the sliding criterion and f_3 is the sliding criterion at high confinement.

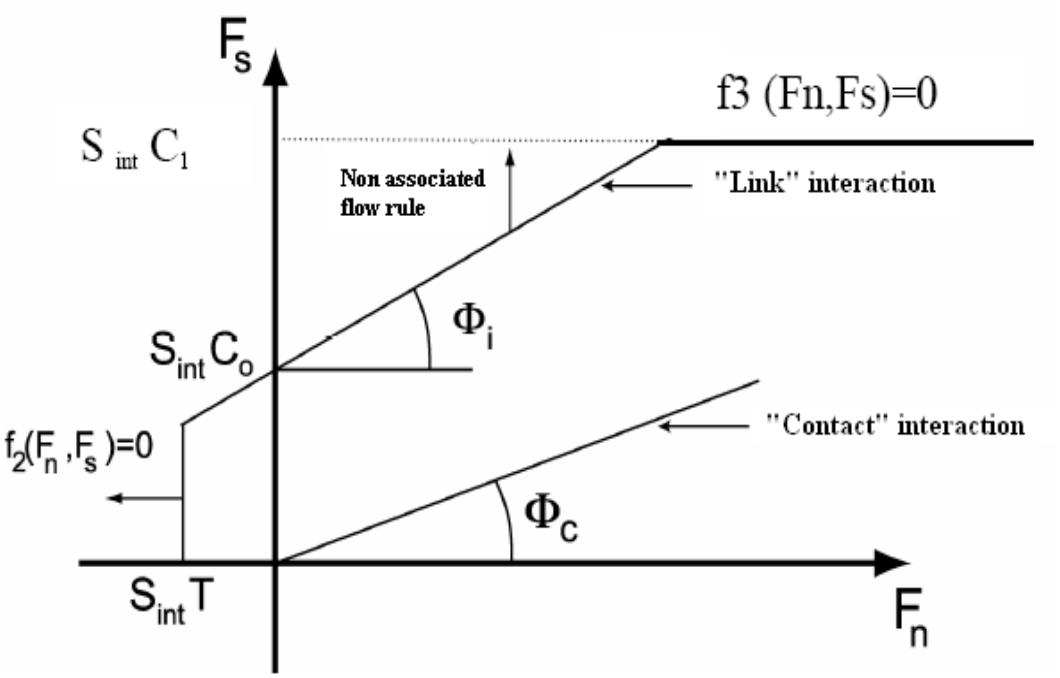

Figure 22 – New rapture criterion

Current interaction radius: The initial interaction radius to determine the initial link of "link" type is determined for a number of internal connections of 12. During the calculation other contact-type connections can be created. Such a link is created when the distance between two discrete elements, not yet linked, becomes less than the current interaction radius. This current interaction radius (taken before equal to one) also affects the results and it is necessary to increase its value to work under very high pressures.

Status of broken links: Initial Links can break in traction. If the discrete elements are distant at the time of rupture of a distance less than the current interaction radius, a contact-type connection will be detected and replace the broken link. This replacement is not desirable because in the previous iteration, the discrete elements were treated in traction. A special procedure has been established. The links of "link" type broken are stored in the list of links with inactive status, which prevents the creation of "contact" type link. We will revive an inactive link (with a "contact" type link) when the distance between the discrete elements is less or equal to the initial distance of the discrete elements. This means that the initial distance taken into account in calculating the deformation of the "contact" type link is the initial distance when it had a "link" type connection. The "contact" type connection will be activated only in a configuration of discrete elements, which would have given a compression behavior for the initial link.

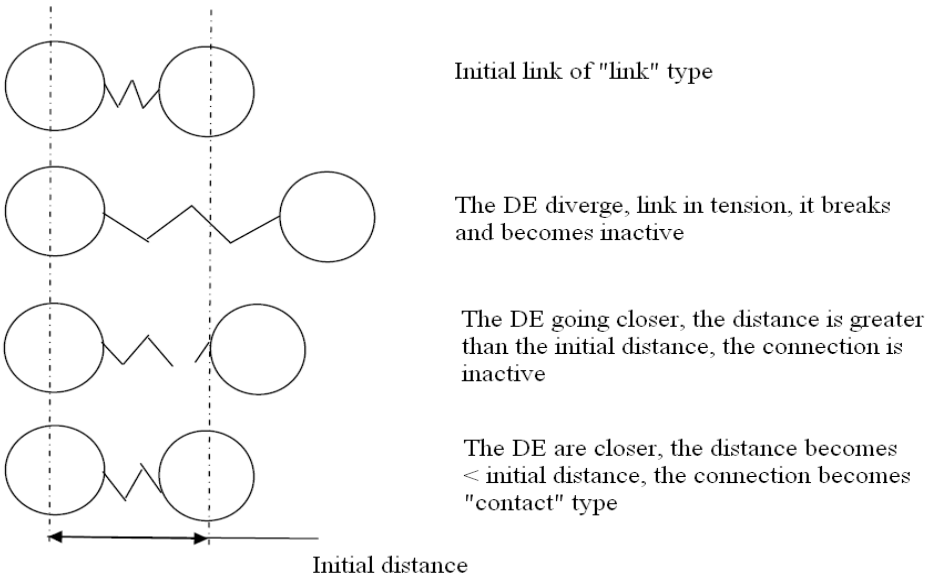

Figure 23 – New rupture criterion

4 Numerical results

4.1 Influence of parameters

It is interesting to study the sensitivity of the behavior of the concrete to each local parameter. This kind of study has been done by Rousseau [2009] and it has been used by us to do a faster calibration of the local parameters. In the followings the main results she has obtained are presented.

Sensitivity to traction: There is a strong dependence of the local behavior of traction to the tensile strength T. An increase of such parameter allows each link to break later causing a higher peak in the curve stress - strain. This kind of behavior is evident during traction tests due to the fact that the links are in tension. Instead in compression, only some links are in traction so increasing tension strength parameter, increase the peak of the curve but not as much as for traction test.

Sensitivity to cohesion: Increasing the value of C_0 we observe that the behavior in traction tests is not affected at all. In compression we have a modification of the curve, that is, an increase of the peak.

Sensitivity to softening: This parameter is very influent both in traction and compression. Increasing it we can observe in traction an increase of the peak with also a modification of the shape of the stress strain curve. Furthermore for high values of softening, before the peak, the slope appears less angular and smoother than for smaller values. We also notice that the post-peak slope is less steep. The softening basically controls the fragility of our materials. The same behavior can be observed in compression test too.

Sensitivity to internal friction angle: Increasing the internal friction angle ϕ_i, the tensile behavior is not influenced but we have a very slight increase of the peak in compression. A little modification is also revealed in the post peak curve that results a bit steeper increasing ϕ_i.

Sensitivity to contact friction angle: This parameter does not reveal any influence over the tensile behavior. This seems reasonable since, as described in *3.1.2*, its effect appears only when, after the break of the cohesive links, the spheres can interact, that is not the case of traction tests. However it affects as well lightly the post-peak in compression because in this phase the links are broken and some links of type “contact” are created between the elements in the damage zone.

These elements revealed in the present and previous works is meant to be a useful guideline for the following works. Apart from the effects of the local parameters we studied also the sensitivity to the number of iterations set in the computations. The results of such study are shown in Figure 24.

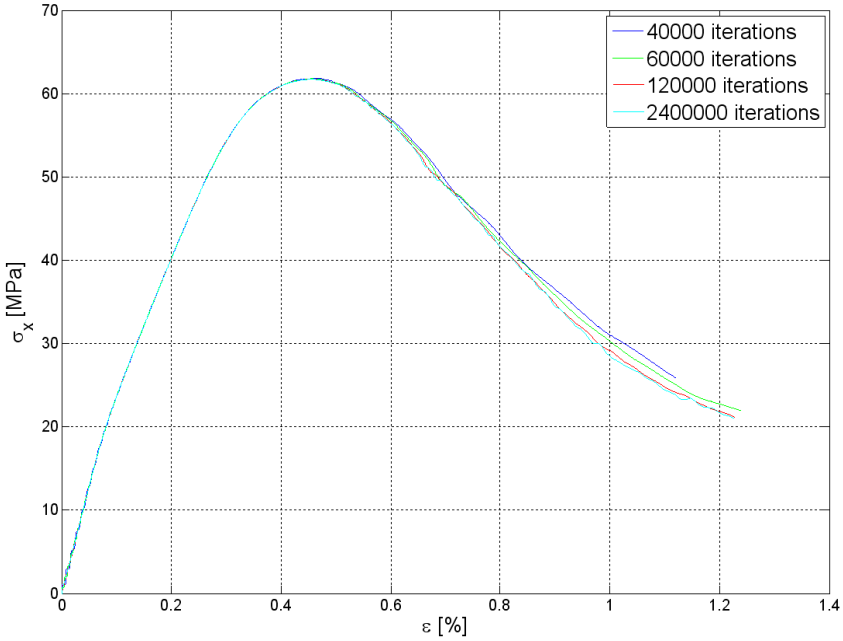

Figure 24 – Sensitivity to the number of iteration

Here we can notice that we do not have any influence on the peak. However increasing the number of iterations we can have a lower velocity and less oscillation in the curve.

4.2 Identification of the parameters

The results explained above allowed us to develop a procedure to identify local parameters. To obtain the macroscopic concrete behavior we did not search directly for concrete parameters. Firstly we search for mortar parameters than for rock parameters and once they are obtained we used them to model concrete.

As it was explained in chapter 3.2.1 to get the microscopic parameter like E and ν we need to identify firstly three parameters: α, β, γ. In our case we use values obtained by Rousseau [2009] that are identified from study of concrete. Rather than identify these parameters for each material taken into account, we have kept α, β, γ of concrete and we have identified the microscopic elastic parameters in order to fit the macroscopic behavior.

The procedure of identification requires several numerical tests of local parameter calibration with respect to macroscopic behavior of concrete in tension and simple compression (Figure 24).

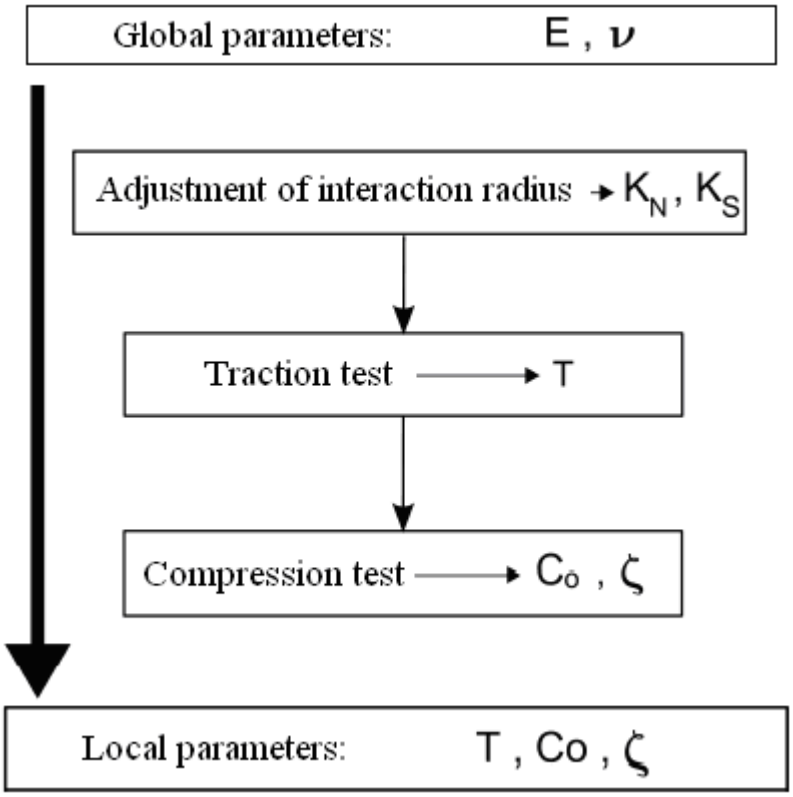

Figure 24 – Identification procedure

The sensitivity tests indicate that the parameters influencing the behavior in traction are the softening ζ and local limit in traction T. Cohesion C_0 has no effect. We can initially identify the parameters ζ and T on a simple tensile test. Once these two parameters are set, we can easily identify the cohesion parameter C_0 with a simple compression test. For rock this identification change a bit due to the fact that for triaxial test at *50 MPa* of confinement the peak is very high and with the value of cohesion identified in the simple compression does not allow us to reach a good peak value. So we have adjusted C_0 to fit the triaxial curve.

As we saw, ϕ_i and ϕ_c do not affect too much the results so we used for mortar the same value identified in Rousseau [2009] for concrete that is equal to *6°* for both. For rock since we want to have a peak in the triaxial test as close as possible to the real one we use the lowest value that does not

modified anymore the increment of the peak and give also a steeper post peak behavior. This value is *60°*.

4.3 Result

In this chapter we are going to verify if the discrete element modelization defined above is able of reproducing a concrete behavior. The section is divided in three main parts. First we are going to discuss calibration for rock, then for mortar and at the end we present results obtain for concrete. The experimental tests of reference are simple compression tests and triaxial tests made in the laboratory 3S-R on mortar MR30A7, on rock and concrete R30A7.

4.3.1 Rock

In this chapter are shown rock parameters. As said in 4.2, after having identified parameters with traction tests and compression tests, we increased the cohesion even more in order to fit the triaxial curve. The parameters obtained are shown in the Table 3.

Parameters	Values
E	58 Gpa
ν	0.02
C0	210 Mpa
T	63 Mpa
ζ	1.00E-04

Table 3 - Rock parameters

The value of softening is chosen very small due to the fact that we want an elastic brittle behavior.
Traction test: Numerical results obtained in this test are shown in Figure 25. Knowing that the real value of T is about *23 MPa* thanks to our calibration we are able to have a proper peak.

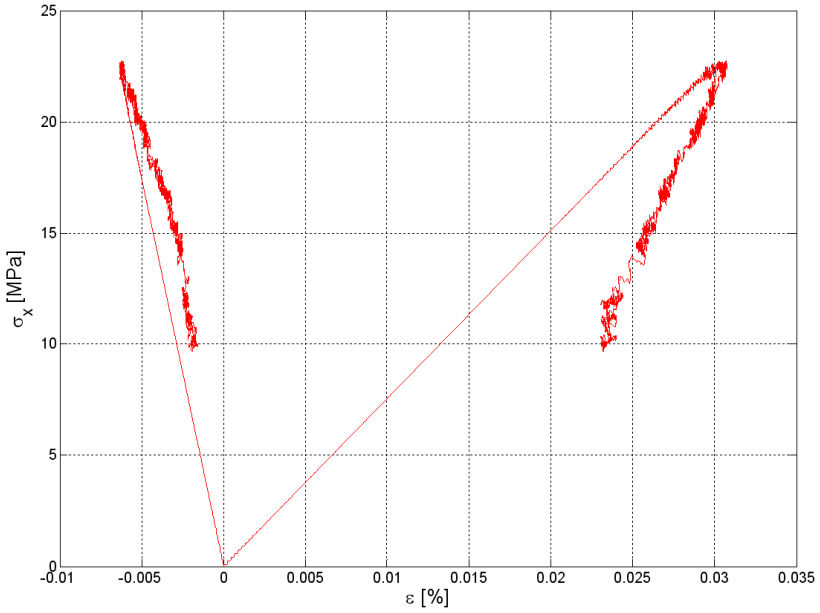

Figure 25 – Traction test

Compression test: For such test the results obtained are shown in Figure 26. It appears that the peak is higher of about *40 MPa*. It happens because the calibration of parameters is done to fit also the triaxial test at *50 MPa* of confinement. To obtain a proper curve also with confinement, we increased the value of cohesion obtaining a higher peak value for both tests. For such reason we can assume the results obtained from simulation in compression quite reasonable.

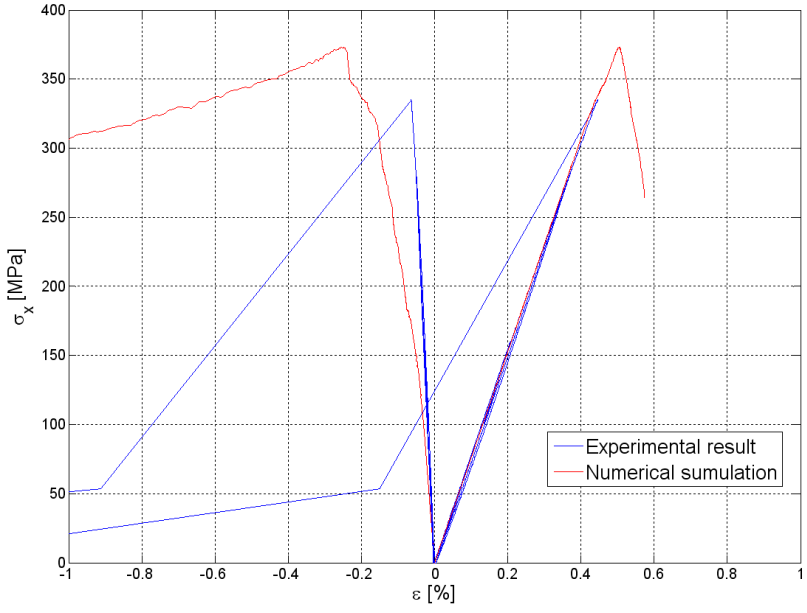

Figure 26 – Compression test

Triaxial test at 50 MPa of confinement: Results obtained with such test are shown in Figure 27. Here are shown two graphs. The first one represents a stress – strain graph with plotted axial and radial strain. We can see that the experimental curve is fitted very well but we can not reach the real peak. The difference is in the order of 120 MPa and it appears very high. However we already know that there is variability in results for experimental tests and in our case we have only one experimental curve. So we can assume that the simulation give also in this case reasonable results. This fact is remarked in the second graph. This time is plotted the volumetric strain and we see that the experimental curve is close to the numerical one and we are also able to reproduce the transition compaction – dilatation.

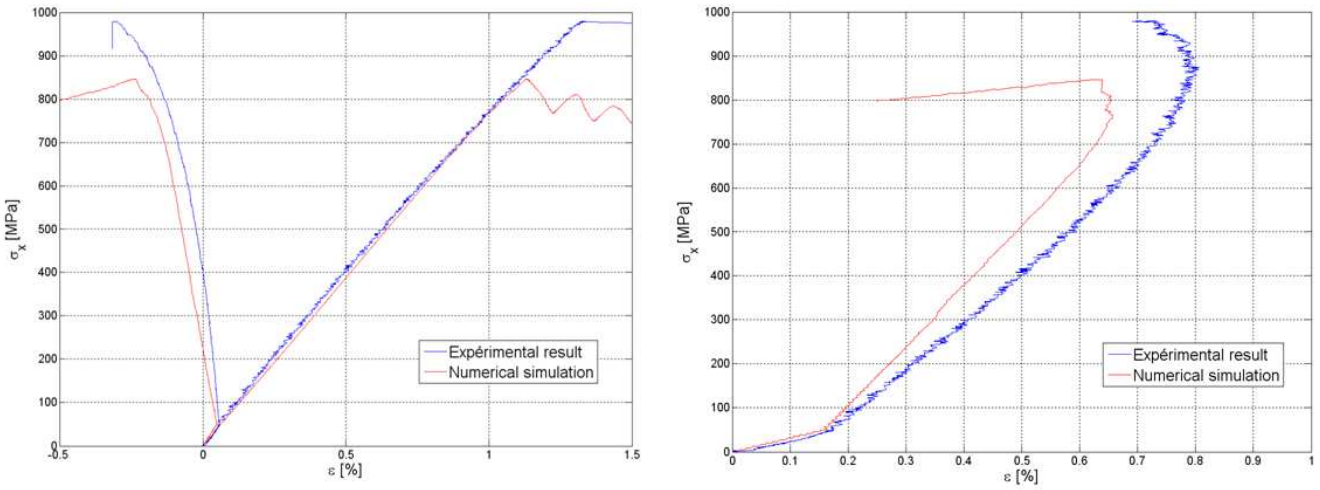

Figure 27 – Triaxial test

4.3.2 Mortar

The procedure adopted is the same as the one used for rock. However, as we are going to see, parameter calibrated on traction and compression tests are already the good ones and they fit well also triaxial curves. In Table 4 are shown the parameters used.

Parameters	Values
E	19 Gpa
ν	0.1
C0	5.5 Mpa
T	9 Mpa
ζ	10

Table 4 – Mortar parameters

Traction test: From Dupray [2008] we know that the value of tensile strength is about 9 MPa. With our simulation we are able to reach a good peak as it is shown in Figure 28. We do not have any experimental curve for traction test so we cannot do assumption about the post peak phase.

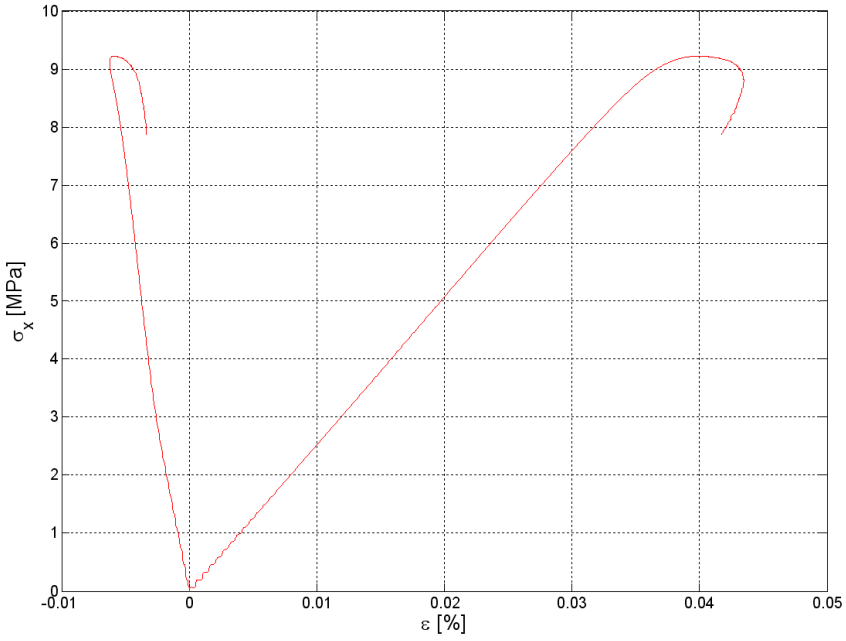

Figure 28 – Traction test

Compression test: Compression test gives the results shown in Figure 29. The experimental behavior is divided in three phases. Firstly we have an elastic phase until *30 MPa*, then appear the non linear behavior with a decreasing of the tangent modulus having a peak at about *60 MPa*. The post peak is characterized by a brittle behavior. Numerical curve reproduces well the pre - peak behavior of mortar. The peak fall perfectly between the two experimental curves and the post peak is not so far from the experimental one.

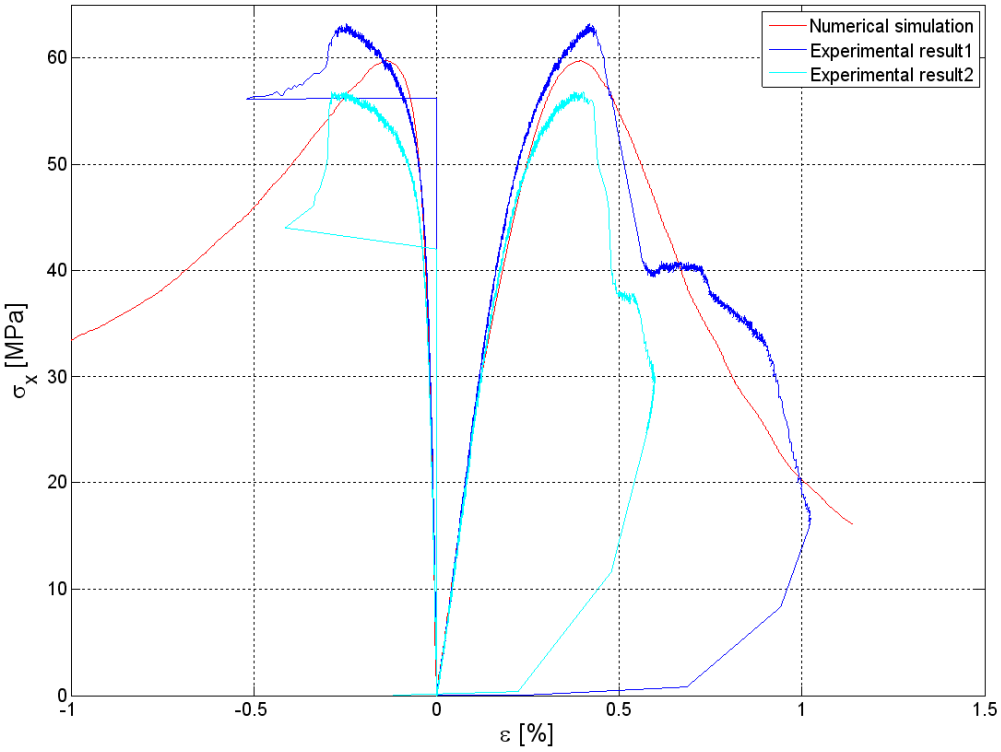

Figure 29 – Compression test

Triaxial tests: Experimental triaxial tests have been done for *60 MPa*, *120 MPa*, *300 MPa* and *650 MPa* of confinement. These curves and as well the numerical curves are plotted in Figure 30. At first view appears clearly that we reproduce well the triaxial behavior. Hydrostatic phase is not so far from the real one and we also have to take into account that the hydrostatic response for numerical test respect the experimental variability. We are also able to reproduce the compactant dilatant phase as it shown in Figure 31. Peaks results slightly higher, except for the case of *60 MPa* of confinement.

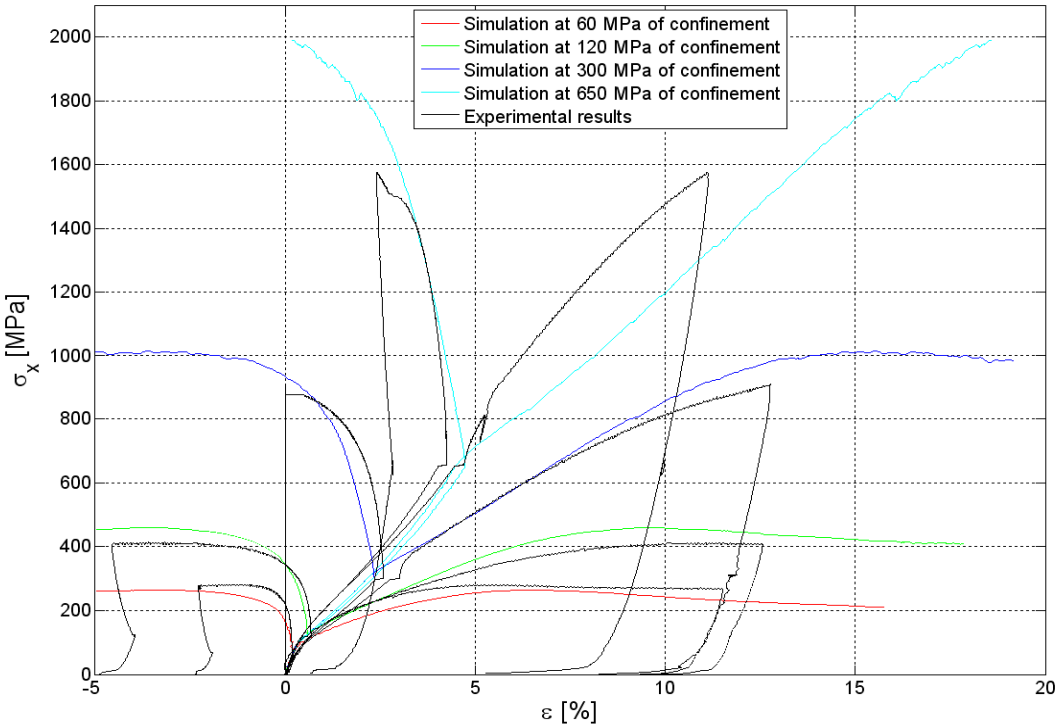

Figure 30 – Triaxial tests (ε_a, ε_r)

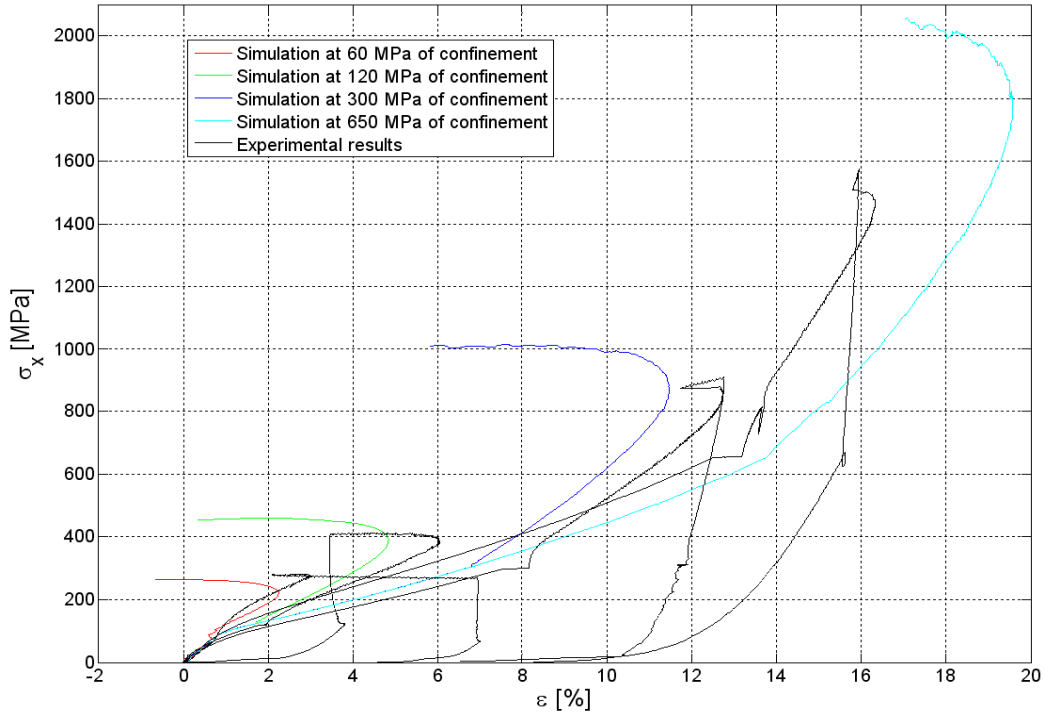

Figure 31 – Triaxial tests (ε_v)

4.3.3 Concrete

As well described previous chapters, we create a numerical sample of concrete that reproduce quite well the reality in term of composition and links. The simulations do not necessity any calibration of parameters. In fact we use for the modelization a file that contain rock and mortar parameters. If these two elements have a good calibration and the mesh reproduce well the reality, results should represent the real macroscopic behavior of concrete.

Traction test: From this test we can see that the peak is higher than the real one that is in the order of *3.5 MPa* and it appears also later at about *0.03 %* of ε_a when the experimental limit of rupture appears at about *0.012 %* of axial strain. The behavior appear also too less brittle than the real one ([Gabet,2006]). At the beginning, in the elastic phase we can avoid the problem of oscillation increasing the number of iterations.

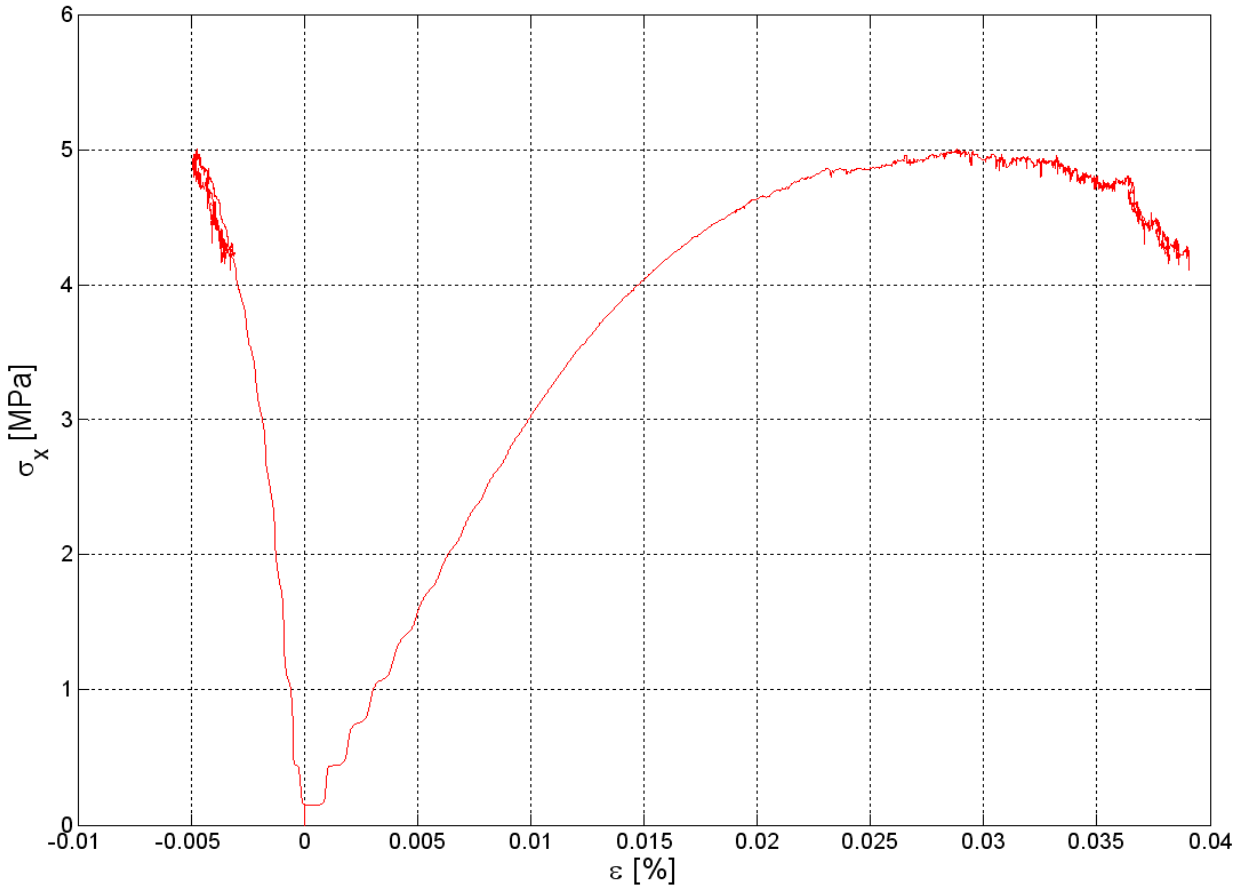

Figure 32 – Traction test

Compression test: Results of compression test are plotted in Figure 33. Experimental tests have been done by C. Poinard and the peak of is reached at *40 MPa* with an axial deformation of 0.2 %. In the simulation we can see that we are not able to reach a proper value in fact we are in the order of *37 MPa* and the non linear behavior appear slightly early.

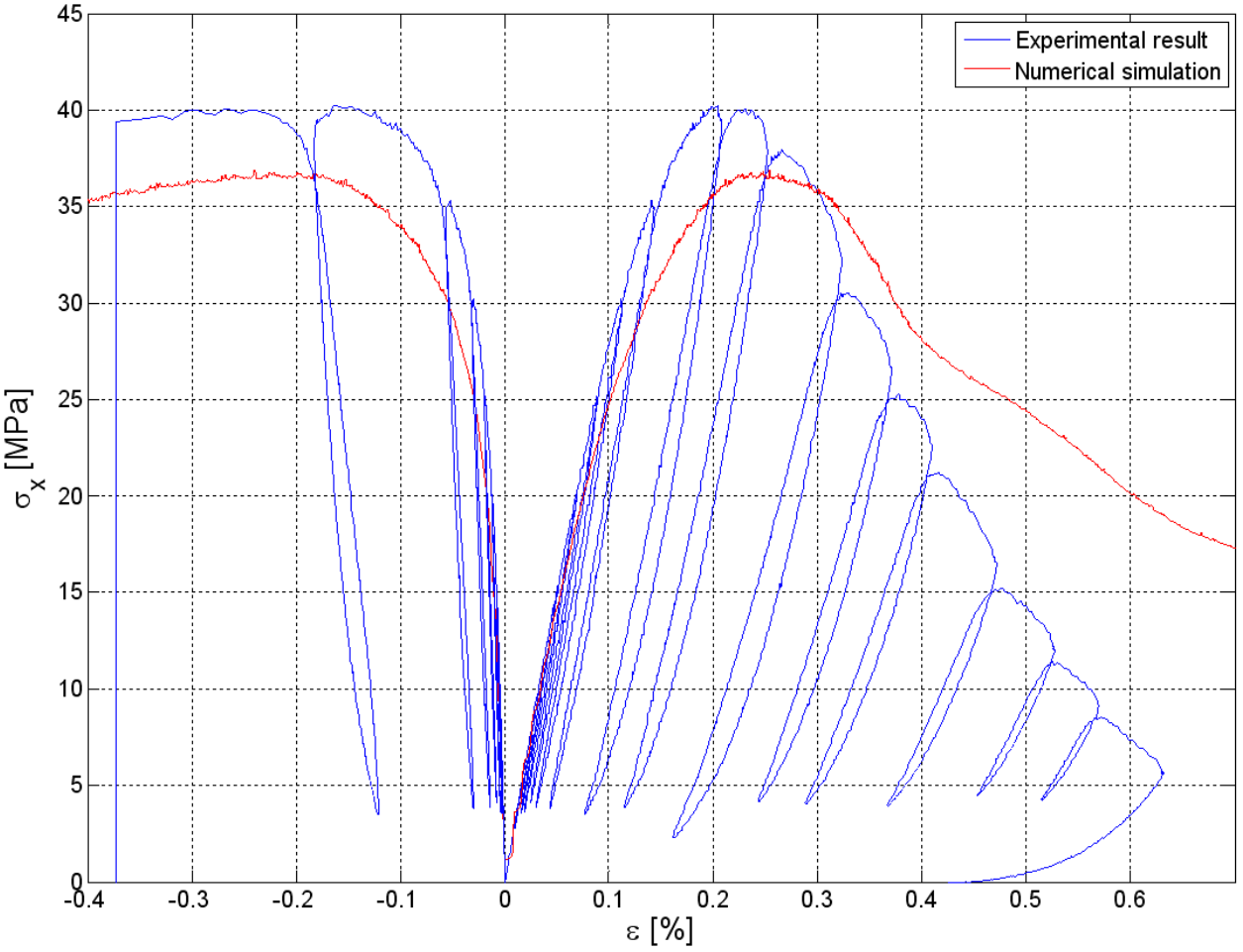

Figure 33 – Compression test

Triaxial tests: Experimental triaxial tests have been done for *50 MPa*, *100 MPa*, *500 MPa* and *650 MPa* of confinement ([Gabet, 2006 and Vu, 2007]). In Figure 30 we have the graph for both experimental and numerical simulation. For triaxial test at *50 MPa* and *100 MPa* of confining pressure we are able to reproduce the experimental results in a good way. Peaks result slightly higher, except for

the case of *60 MPa* of confinement. For the hydrostatic phase the same assumption made for mortar can be done concrete. We can add the fact that in the real case we have an underestimation of the air bubble porosity and this gave us a steeper hydrostatic part. We are also able to reproduce the compactant dilatant phase as it shown in Figure 31. However for high confinement results are a bit far from the experimental curves.

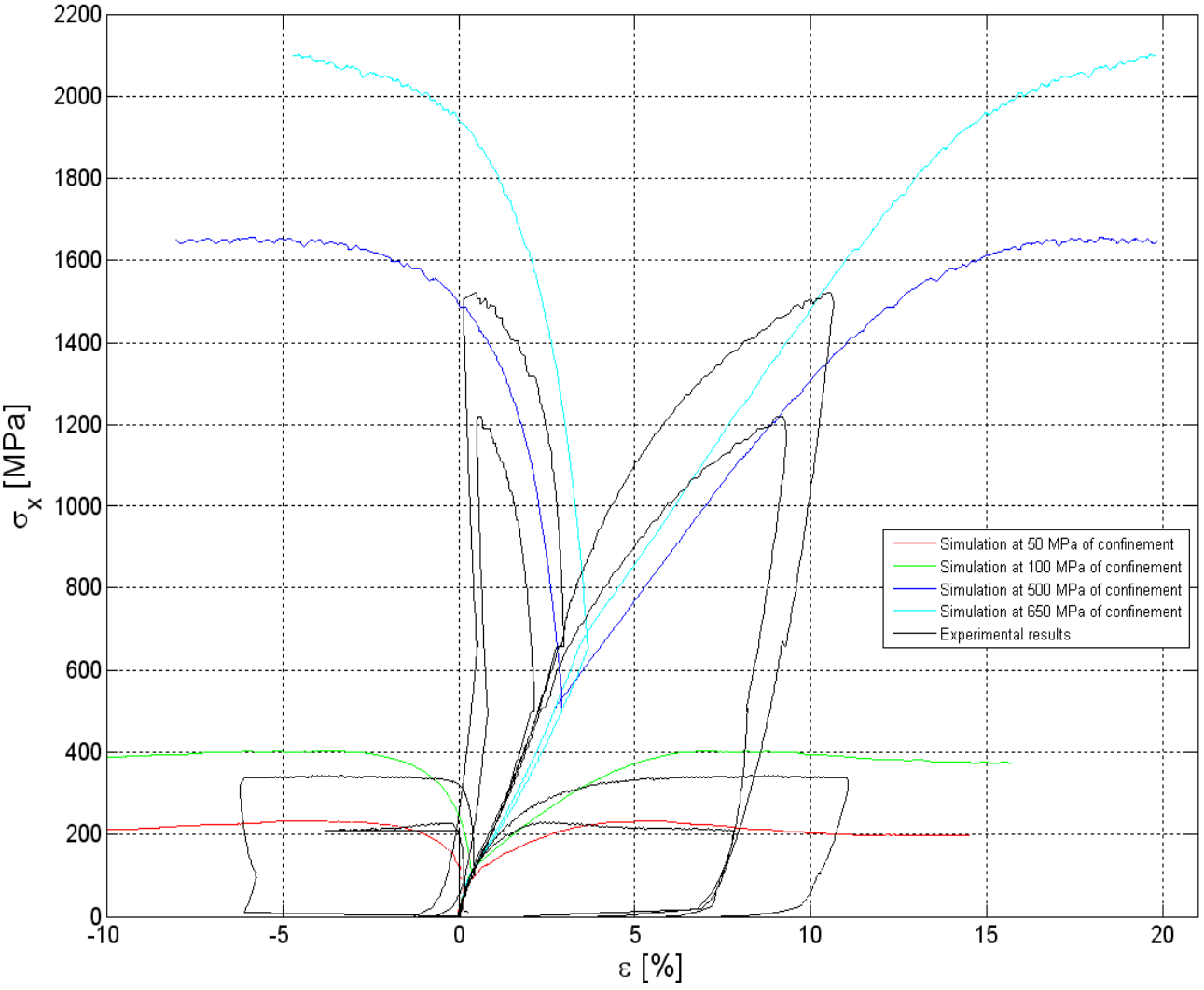

Figure 34 - Triaxial tests (ε_a, ε_r)

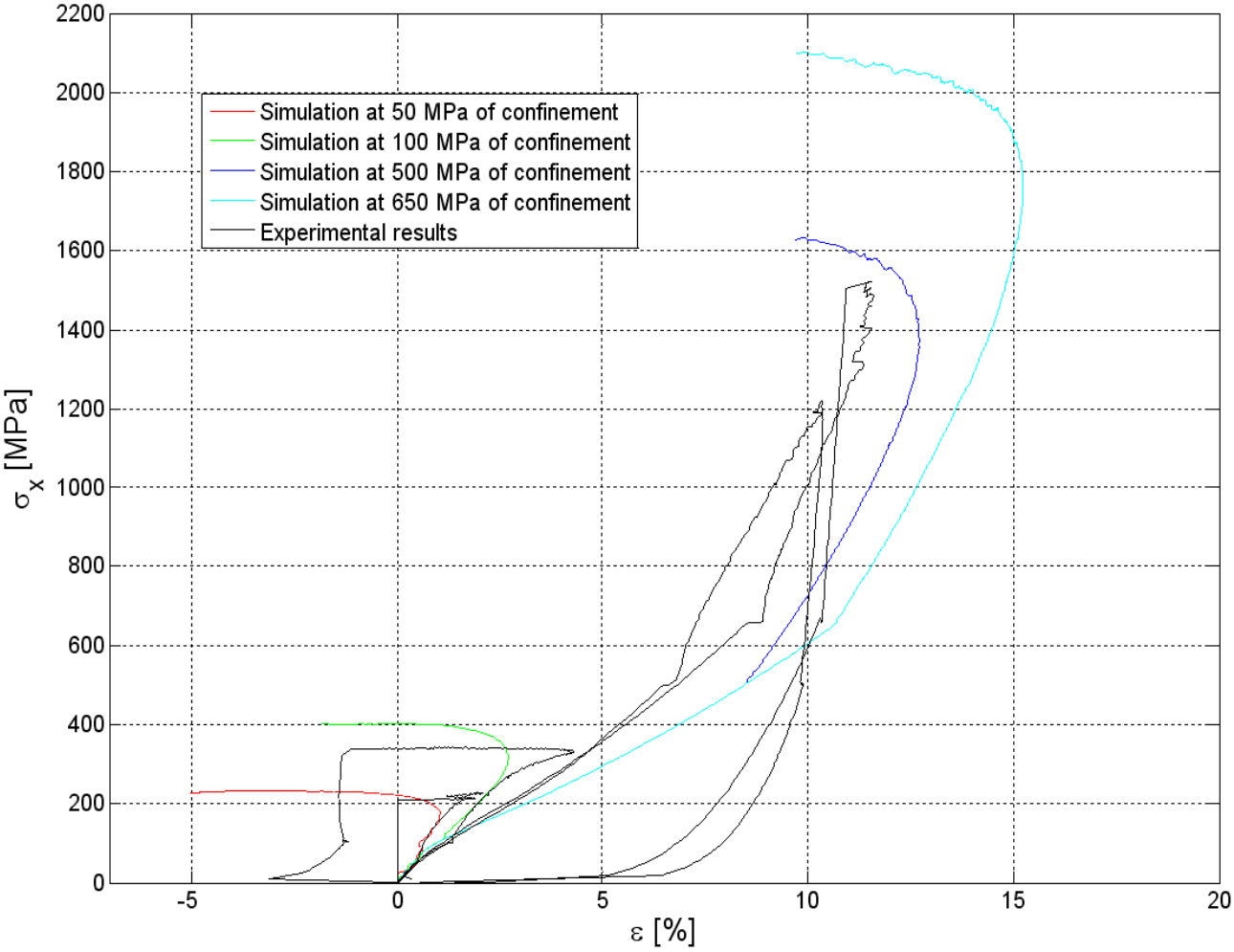

Figure 35 - Triaxial tests (ε_r)

5 Conclusions

The study realized has allowed us to create a new numerical sample that takes into account the heterogeneity of the material. In order to reproduce the macroscopic behavior of concrete we have done several simulations on the two elements inside it: mortar and rock. Thanks to the parameters found for them we are able now to reproduce with good approximation the macroscopic behavior of concrete. However we have seen that there are still differences between experimental and numerical results. This work can be seen as a good starting point for a larger work. There are many things that can be improved. Firstly the future worker has to focus his study on the repartition of links between each element in order to have a better description of the real sample. It is also important to find a proper parameter (see chapter *2.4.3*) for the interaction mortar – aggregate. In our case we have not had enough time to calibrate it in a proper way. Then it is necessary to improve the calibration specially to fit better triaxial curve at high confinement for mortar. Another important point is to improve the hydrostatic phase trying to find better parameters *a*, *b*, *c* described in *3.2.3*. Then it should be interesting to see the global damage of the specimen and improve the identification of it where the damage in our computation is given by $\frac{broken\ links}{total\ links}$ for each sphere. This is useful to make an interesting comparison with the experimental result. Inside this kind of work could be also good to see what happen instead for each phase, mortar and aggregate, inside the concrete sample.

In the end we have to pay attention that also in the case studied in this work all the results can be improved even more increasing the number of spheres of the mesh. The drawback of this is that simulations, that have taken already long computation time in the case studied, are going to take even much more time and work could be too long.

Bibliography

BAILLY, P., TOMBINI, C. et LE VU, O. (1996). Modélisation de géomatériaux sous sollicitations dynamiques élevées. i : Un tir de pénétration sur cible en béton. *In Colloque du réseau GEO*, Aussois, France. 1

CEG/DGA et 3S-R (2007). Caractérisation et modélisation du comportement mécanique des bétons sous très fort confinement. Rapport final contrat d'études et de recherches, CEG/DGA 3S-R. 24

CUNDALL, P. et STRACK, O. (1979). A discrete numerical model for granular assemblies. *Geotechnique*, *vol 29 n°1 pp 47-65. 13*

DUPRAY, F (2008). Comportement du béton sous fort confinement : Etude en compression et en extension triaxiales à l'échelle mésoscopique. 2, 35

GABET, T. (2006). *Comportement triaxial du béton sous fortes contraintes : Influence du trajet de chargement*. Thèse de doctorat, Laboratoire 3S-R. 2, 38, 39

GÉRADIN, M. et RIXEN, D. (1993). *Théorie des vibrations, application à la dynamique des structures*. Masson. 20

HENTZ, S. (2003). *Modélisation d'une Structure en Béton Armé Soumise à un Choc par la méthode des Éléments Discrets*. Thèse de doctorat, Université Joseph Fourier. 17,22

JENSEN, R., BOSSCHER, P., PLESCHA, M. et EDIL, T. (1999). Dem simulation of granular media - structure interface: effect of surface roughness and particle shape. *Int. Journal Num. Anal. Meth. Geomec. 23:531–547.* 14

JERIER, J.-F., IMBAULT, D., DONZE', F.-V. et DOREMUS, P. (2008). A geometric algorithm based on tetrahedral meshes to generate a dense polydisperse sphere packing. *Granular Matter*. in press. 5

PLASSIARD, J.-P. (2007). *Modélisation par la méthode des éléments discrets d'impacts de blocs rocheux sur structures de protection type merlons*. Thèse de doctorat, université Joseph Fourier, Grenoble. 14

ROUSSEAU, J (2009). *Modélisation numérique du comportement dynamique de structures sous impact sévère avec un couplage éléments discrets / éléments finis*. Thèse de doctorat, université Joseph Fourier, Grenoble. 2, 13, 23, 29, 30, 31

SALOT, C. (2007). *Modélisation du comportement mécanique d'un matériau granulaire compositepar la méthode des éléments discrets*. Thèse de doctorat, Université Joseph Fourier. 14

VU, X. H. (2007). *Caractérisation expérimentale du béton sous fort confinement : influence du degré de saturation et du rapport eau/ciment*. Thèse de doctorat, Laboratoire 3S-R. 2, 39

ZUKAS, J. A. (1992). *Impact Dynamics*. Krieger. 1